climate

MDPI

Article

Variability and Changes in Temperature, Precipitation and Snow in the Desaguadero-Salado-Chadileuvú-Curacó Basin, Argentina

Gabriela V. Müller [1,2,*] and Miguel A. Lovino [1,2]

[1] Consejo Nacional de Investigaciones Científicas y Técnicas (CONICET), Buenos Aires 1425, Argentina; mlovino@unl.edu.ar
[2] Centro de Estudios de Variabilidad y Cambio Climático (CEVARCAM), Facultad de Ingeniería y Ciencias Hídricas, Universidad Nacional del Litoral, Santa Fe 3000, Argentina
* Correspondence: gvmuller@fich.unl.edu.ar

Abstract: We analyze the variability and changes in mean temperature, annual precipitation, and snow water equivalent (SWE) in the Desaguadero-Salado-Chadileuvú-Curacó (DSCC) basin, observed in a recent period, and their projected future values. The current climate and observed changes are studied based on the scarce observation records available in the region. Simulations from the High-Resolution Model Intercomparison Project (HighResMIP v1.0) are used for the analysis of future climate projections. The mean annual temperature presents a major rise between 1 and 2 °C throughout the region in the 1961–2020 period. The annual precipitation has nonlinear positive trends of varied importance. The SWE has decreased noticeably since 2010. Interannual variability also plays a key role, with dominant cycles between 2.8 and 4 years and between 7.5 and 10 years. The projected changes, computed as the difference between the 1985–2014 and 2021–2050 averages, reveal a rise in mean annual temperature in the entire basin, with an eastward magnitude increase from 1 to more than 2 °C. The annual precipitation is projected to increase up to 10% over most of the basin, except in the Andes, where it will decrease. The maximum annual SWE will also continue to decrease, in agreement with the trend observed in recent years.

Keywords: climate change; precipitation; temperature; snow; Desaguadero-Salado-Chadileuvú-Curacó basin

Citation: Müller, G.V.; Lovino, M.A. Variability and Changes in Temperature, Precipitation, and Snow in the Desaguadero-Salado-Chadileuvú-Curacó Basin, Argentina. *Climate* **2023**, *11*, 135. https://doi.org/10.3390/cli11070135

Academic Editor: Junqiang Yao

Received: 6 May 2023
Revised: 9 June 2023
Accepted: 12 June 2023
Published: 26 June 2023

1. Introduction

The observed climate changes on a global scale in recent decades show the need to understand the regional-scale impacts of those changes, mainly those associated with increased or decreased water availability. Water availability depends on precipitation, which presents increasingly extreme deficits and excesses. In South America, the lack of precipitation in some regions has caused long-lasting and persistent droughts [1,2], while other regions present frequent floods caused by extreme precipitation events [3,4]. For example, a continuous rainfall decline has been recorded in central Chile from 2010 to the present [5,6]. On the other hand, increased heavy precipitation events favored frequent floods in southeastern South America during the 2000s [7–9].

In arid to semiarid regions of the world, water availability is facing more recurrent reductions [10,11]. In particular, central-western Argentina has undergone a sustained increase in the annual mean temperature, an increase in annual precipitation and in the frequency of extreme precipitation events towards the eastern lowlands of the region, and a sustained precipitation decline over the Andes [11–13]. This declining precipitation favors decreases in snow accumulation and, consequently, streamflow droughts [14,15]. Since the snowmelt feeds the main rivers in the central-western Argentina region, this

reduction in snow volume causes severe difficulties for the management of scarce water resources [11]. Future projections indicate that the Andes region is expected to experience more marked temperature increases [16,17]. Furthermore, the observed decline in precipitation since the last century is projected to persist, leading to an increased frequency of drought conditions [13,18,19]. The combination of reduced precipitation and increasing temperatures will contribute to glacier mass balance losses and trigger premature snowpack melting, which poses significant challenges for water management [17,20].

There are several forcing factors associated with the changes and variability in the water cycle over central-western Argentina [21]. For example, the long-term reduction in winter precipitation, mainly over the Andes, was favored by a poleward expansion of the Hadley circulation that led to a southward displacement of the semipermanent South Pacific anticyclone [22]. This expansion was attributed mainly to increased greenhouse gas emissions, ozone depletion effects, and internal climate variability [23,24]. One of the main climatic forces that modulates interannual hydroclimate variability is the El Niño–Southern Oscillation (ENSO) [13,25,26]. Precipitation and streamflow present positive anomalies during El Niño years, while La Niña years favor reduced snowfall and potential streamflow drought conditions [26,27].

In particular, the Desaguadero-Salado-Chadileuvú-Curacó basin, located in central-western Argentina, presents high vulnerability to climate variability and climate change due to (1) the complex system of water resources on which all socioeconomic activities in the region depend, (2) the changes in the hydrological cycle that have occurred in recent decades [13,16], and (3) the large population that the basin encompasses (approximately 3.5 million inhabitants) [28]. According to [28], the main critical situations that occur in the basin are associated with floods and droughts of various origins, as well as processes of salinization, erosion, and environmental contamination favored by anthropic processes. For this reason, an in-depth analysis of the climate variability and change that affect regional hydrological processes is required in the entire basin in order to specify water policies and strategic interventions to favor an integrated management of the complex water system.

In this study, we analyze the mean characteristics, variability, and changes in temperature, precipitation, and snow precipitation (by means of the snow water equivalent) in the Desaguadero-Salado-Chadileuvú-Curacó basin over a historical period, and provide projections for the future climate. Section 2 describes the data and methodology. The results are presented in Section 3, and the discussion and conclusions are presented in Section 4.

2. Data and Methods

2.1. Study Region

The study region includes the Desaguadero-Salado-Chadileuvú-Curacó (DSCC) basin, which stretches across the central Andes and part of the central region of Argentina and discharges towards southern Buenos Aires (Figure 1a). The DSCC system covers 360,000 km^2 and constitutes the set of basins and hydric regions with the largest area fully developed within Argentina [28]. The basin runs from north to south along an arid and semiarid strip of 1000 km in length in a complex hydrographic system, with a very complex topography (Figure 1b). The system develops from the Andes, with elevations above 5000 m, and drains into the Atlantic Ocean, crossing the central plain of Argentina through the Colorado River. The Desaguadero river, the river that drains most of the basin area in central-western Argentina, receives its main tributaries that originate from the melting of the Andes. For this reason, and due to the scarce precipitation registered in the extensive territory that it covers, its maximum streamflow occurs at the end of spring [28].

The precipitation seasonality is markedly different in the Andes mountains and in the lowlands, situated east of the Andes [13]. The Andes region experiences a Mediterranean regime, characterized by a wet and cold season from April to September, followed

by a dry and warm season from October to March [29]. In contrast, the lowlands region exhibits a monsoonal precipitation regime. In the western part of the lowlands, where the seasonality is more pronounced, an arid to semiarid climate prevails [30]. On the other hand, the eastern portion of the lowlands has a subhumid climate [31].

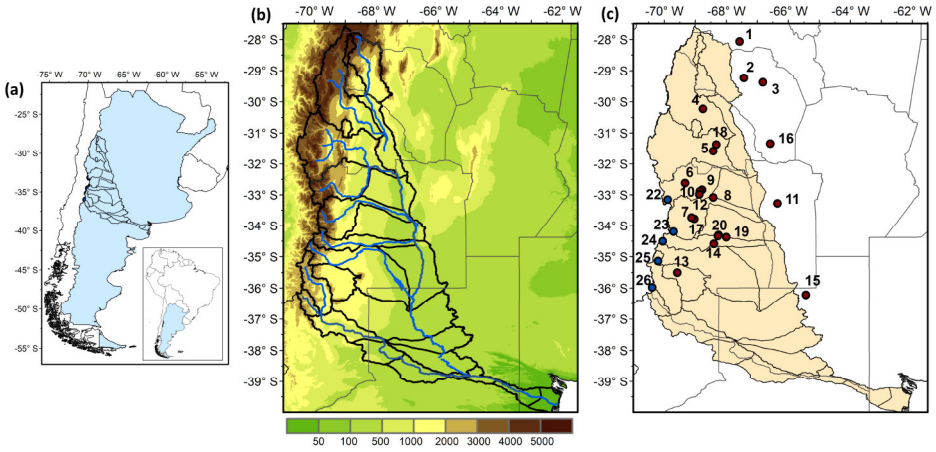

Figure 1. (**a**) Location of the Desaguadero-Salado-Chadileuvú-Curacó basin in Argentina. (**b**) Topography map of the study region along with the main rivers. The solid black lines highlight the main sub-basins. (**c**) Spatial distribution of stations with long records of high-quality datasets of observed precipitation and temperature (red points) and snow water equivalent (blue points). See station characteristics in Table 1.

Table 1. Stations with temperature, precipitation, and snow data. The percentage of missing data indicates the number of months without data in the 1961–2020 and 1995–2014 periods. The stations included in this study are shaded in grey. Color shading highlights stations with less than 10% missing data in the 1961–2020 period for temperature (light blue) and for precipitation (green).

#	Station	Lat	Lon	masl	Missing Values 1961–2020 (%)		Missing Values 1995–2014 (%)		
					Tmean	PP	Tmean	PP	Snow
1	Tinogasta	−28.07	−67.57	1201	4.3	10.3	0.0	0.0	
2	Chilecito Aero	−29.24	−67.43	945	64.4	40.8	84.6	0.0	
3	La Rioja Aero	−29.38	−66.82	429	3.8	0.6	0.0	0.0	
4	Jáchal	−30.23	−68.75	1175	4.7	11.9	0.0	0.0	
5	San Juan Aero	−31.58	−68.42	598	3.5	3.6	0.0	0.0	
6	Uspallata	−32.62	−69.33	1891	27.9	57.1	12.9	29.2	
7	San Carlos	−33.78	−69.03	940	8.8	54.2	0.0	---	
8	San Martín	−33.09	−68.42	653	1.4	1.0	0.0	0.0	
9	Mendoza Aero	−32.84	−68.78	704	3.5	0.0	0.0	0.0	
10	Mendoza Obs	−32.89	−68.85	827	5.3	0.3	0.0	0.0	
11	San Luis Aero	−33.28	−66.35	713	1.9	0.8	0.0	0.0	
12	Chacras de Coria	−32.99	−68.87	921	6.0	14.3	0.0	8.0	
13	Malargüe Aero	−35.51	−69.58	1425	4.4	0.4	0.0	0.0	
14	San Rafael Aero	−34.59	−68.40	748	0.6	0.1	0.0	0.0	
15	Victorica	−36.22	−65.43	312	30.8	35.4	16.7	21.3	
16	Chepes	−31.34	−66.58	658	29.7	19.3	42.9	25.8	
17	La Consulta	−33.74	−69.12	940			0.4	0.0	
18	Pocito	−31.37	−68.32	618			0.4	0.0	
19	La Llave	−34.38	−68.00	555			25.8	16.7	
20	Las Paredes	−34.31	−68.25	813			21.3	17.1	

21	Capitán Montoya	−34.34	−68.27	791	---	0.0
			Stations with snow data			
22	Toscas	−33.16	−69.89	3000		31.4
23	Laguna Diamante	−34.2	−69.70	3301		10.7
24	Laguna Atuel	−34.51	−70.05	3423		12.9
25	Paso Pehuenche	−35.14	−70.20	2253		33.6
26	Valle Hermoso	−35.98	−70.39	2555		11.4

2.2. Observed Data

Figure 1c shows the meteorological stations located in the study region as well as the areas lacking observations, which are located mainly the southernmost portion of the basin. The spatial observation coverage is limited. The variables analyzed were maximum, minimum, and mean daily temperature; daily precipitation; and the snow water equivalent (SWE). The mean daily temperature was calculated as the average between the minimum and maximum daily values. SWE represents the water column that would result from melting the entire snow layer instantaneously.

Data quality was tested using quality control techniques, including overall control, fixed range, temporal continuity, and spatial consistency. We identified the stations with the longest records of temperature and precipitation (Table 1). The period common to these stations extends from 1961 to 2020. As shown in Table 1, although several stations have a long observation period, they present numerous data gaps. The monthly temperature and precipitation series with longest records used in this study are those presenting less than 10% missing data. Table 1 shows the completed series; color shading indicates stations meeting the mentioned criterion (light blue: 12 stations for temperature; green: 8 stations for precipitation).

The data gaps in the selected time series were then filled. The months presenting more than 20% missing days were excluded from the analysis. Missing monthly values were filled with the average of the corresponding month [32], here calculated using 5 consecutive years centered on the year of the missing month. This method guarantees minimum impact on long-term trends [32]. When missing values corresponded to the two first or last years in the series, the average was calculated with the first or last five years, respectively. This method worked correctly, as missing data corresponded to separate years.

The period common to the three variables of interest is 1995–2014. The analysis included the stations with at least 80% of monthly data in this time period. For the climatological analysis, we incorporated additional stations to those previously selected. Additional stations were La Llave and Las Paredes, which fail to meet the temperature criterion by only a small percentage, and San Carlos and Capitán Montoya, which only have temperature and precipitation observations, respectively. The stations included in the analysis are shaded in grey in Table 1. Although Mendoza Observatorio station has a complete set of observations, it is not included in the analysis because we used data from Mendoza Aero, which is very close to it.

Table 1 also shows the five available stations located in the higher elevations of the Andes used for the SWE analysis (Figure 1b,c). SWE is measured directly by "weighing" snowfall using snow pillows. This measurement is more accurate than the product of the depth of the snow cover and its density. Snow depth can vary greatly from hour to hour, due to settlement and compaction, but the amount of water contained within the snow remains constant. Although the data quality was verified by the General Department of Irrigation of Mendoza province (Argentina), [33] reported that several issues, including budget limitations or difficulty in accessing the sites, have affected the frequency and time of snow measurements.

2.3. Simulated Data

This study used five high-resolution models from the High-Resolution Model Intercomparison Project (HighResMIP v1.0; [34]) from the Coupled Model Intercomparison Project Phase 6 (CMIP6; [35]) (Table 2). The models were selected because they are the only ones that have both historical and future simulations available. We used the coupled historic runs for the period 1950–2014 (hist-1950) and coupled scenario simulations for 2015–2050 (highres-future), the latter of which are effectively a continuation of the historic simulation into the future [34]. The analyzed variables included monthly mean temperature, monthly precipitation, and monthly SWE. Model resolution ranges between 0.23° and 0.5° latitude and longitude and allows a more accurate definition of the study region's complex topography. These high-resolution models provide improved representation compared with that of the original low-spatial-resolution models.

The spatial distribution of the changes in mean annual temperature and annual precipitation between the 2021–2050 and 1985–2014 periods was determined. These changes were calculated for each model in its original spatial resolution and for the multi-model ensemble with a resolution interpolated to 0.5° of latitude and longitude, for which the bilinear interpolation method was used (as in [22] and [36]).

Table 2. High-resolution general circulation models from the HighResMIP v1.0 used in this study, their institutions, and their atmospheric resolutions.

	Model	**Institution, Country**	**Atmospheric Resolution (°lon × °lat)**
1	EC-Earth3P-HR *	EC-Earth Consortium	0.35 × 0.35
2	CNRM-CM6-1-HR *	CNRM-CERFACS, France	0.5 × 0.5
3	HadGEM3-GC31-HM	MOHC, UK	0.35 × 0.235
4	CMCC-CM2-VHR4	CMCC, Italy	0.31 × 0.23
5	HiRAM-SIT-HR	AS-RCEC, Taiwan	0.23 × 0.23

* indicates models with snow water equivalent data.

2.4. Singular Spectrum Analysis

Singular spectrum analysis (SSA; [37,38]) was applied to detect long-term changes as well as variability at multiple scales (from interannual to decadal) in the time series of mean annual temperature and annual precipitation. SSA determines the spatiotemporal structures of trends and oscillatory modes in the series. The SSA method performs an eigenvalue decomposition into temporal-empirical orthogonal functions (T-EOFs, eigenvectors) and temporal-principal components (T-PCs). Each T-PC denotes a filtered version of the original time series, explaining a portion of its variance associated with its corresponding eigenvalue. A cycle can be found when two consecutive eigenvalues are close to equal and their related T-PCs are in quadrature. A nonlinear trend is found when the estimation error of a leading eigenvalue, computed following [39], does not overlap with other eigenvalues and its corresponding T-PC is slowly varying and uncorrelated with other T-PCs [38,40].

The choice of the window length M is critical; it limits the longer periods that the SSA can resolve. In this study, we used a window length of M = 10 years that represents interannual variability within the spectrum between 2 and 10 years. Our analysis thus focuses on nonlinear trends and interannual variability modes.

Finally, a Monte Carlo method [41] was used to test mode significance at the 95% confidence level against a red noise null hypothesis with an ensemble of 1000 independent realizations. In this study, SSA was applied to the longest and most complete time series over the 1961–2020 period. We did not apply SSA to SWE time series because they have short time periods, beginning in the early 1990s.

2.5. Evaluation and Bias-Correction Methods

The ability of the GCMs to represent temperature, precipitation, and SWE was assessed by means of statistical evaluation metrics, such as the root-mean-square error (RMSE), the mean bias error (MBE), and the Pearson's correlation coefficient (r) (see [42] for definitions). Statistical evaluation metrics were calculated for each variable at the stations with long-term records. The periods analyzed are the longest available at each station. We present the results of individual models and multi-model ensembles. The ensembles include all the models used.

We applied a scaling method [43] to correct systematic errors of the GCMs and to fit simulated variables to the observed time series. This method uses the ratio between the observed and simulated mean variables for the period estimated in the historical scenario as a scaling factor (Equation (1)). Thus, the corrected variable y_i^p at time *i* is represented by the modeled variable $x_{mod,i}^p$ at time i, scaled with the ratio of the mean observed variable $\bar{y}_{obs}^p$ and the mean modeled variable $\bar{x}_{mod}^p$.

$$y_i^p = x_{mod,i}^p \frac{\bar{y}_{obs}^p}{\bar{x}_{mod}^p} \quad (1)$$

The scaling method was applied to both historical and future simulations. Historical simulations were corrected using the observed data as $\bar{y}_{obs}^p$, such that the MBE of the bias-corrected time series became zero. Future simulations were corrected using the same scaling factor used for historical simulations:

$$y_i^f = x_{mod,i}^f \frac{\bar{y}_{obs}^p}{\bar{x}_{mod}^p} \quad (2)$$

where f indicates the future and p means the past.

3. Results

3.1. Climatology

Figure 2 shows the mean annual temperature (Figure 2a) and annual precipitation (Figure 2b) in the 1995–2014 period at the stations shaded in light blue in Table 1. The mean annual temperature varies from 12–14 °C towards the southwest to 20–22 °C towards the northeast. Note that some stations are beyond the basin, but they are the only observational references in that region. Annual precipitation ranges from 90–100 mm in the arid center of the basin (the San Juan Aero and Pocito stations) to 300–400 mm towards the south (e.g., Malargüe Aero), yet it reaches 687 mm at San Luis Aero. Although the latter station is located beyond the basin, it is very close to its east boundaries. Thus, the precipitation regime is arid to semiarid towards the west of the DSCC basin and the east of the Andes, and subhumid towards the east of the basin. Annual precipitation presents a large spatiotemporal variability, which is conditioned by not only geographic, but also topographic characteristics, such as elevation, slope, and aspect.

Figure 2c,d present the annual mean and maximum SWE, respectively, over the 1995–2014 period. The lowest climatological values are observed at the stations towards the north—Toscas and Laguna Diamante—with 284 mm and 354 mm, respectively. The climatological peak occurs at Laguna Atuel with 902 mm. Farther to the south, the Paso Pehuenche and Valle Hermoso stations have climatological SWEs of 736 mm and 624 mm, respectively. The averages of the annual peaks of SWE in the study period have the same spatial distribution as the mean annual SWE, although with slightly higher values. The annual maximum SWE ranges between 353 mm and 1101 mm.

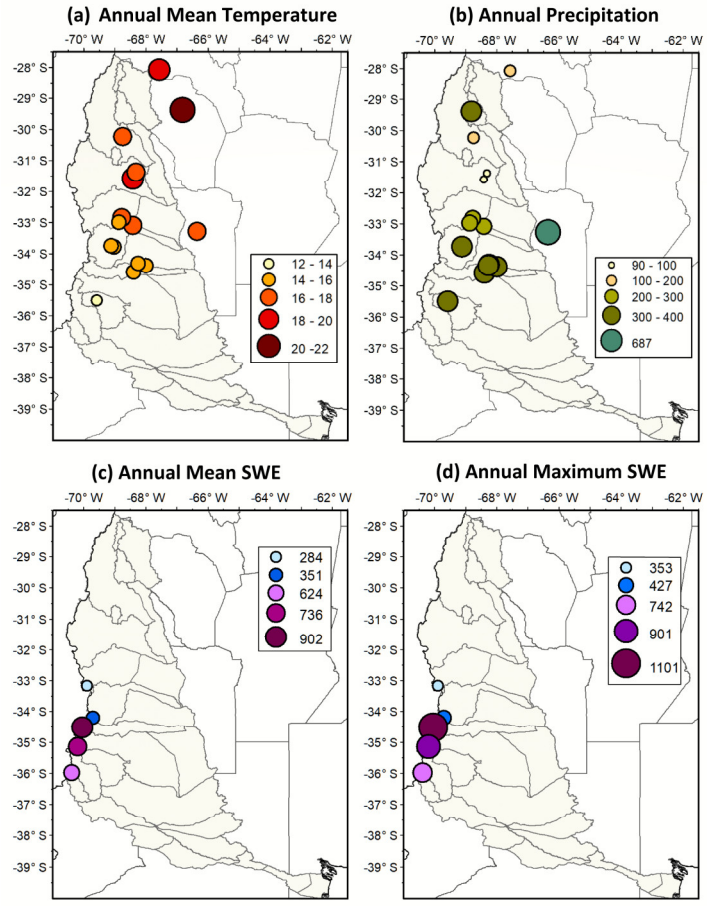

Figure 2. Climatological values over the 1995–2014 period of (**a**) annual mean temperature, (**b**) annual precipitation, (**c**) annual mean SWE, and (**d**) annual maximum SWE.

Figure 3 exhibits the annual cycles of mean monthly temperature (blue lines) and monthly precipitation (green bars) in the 1995–2014 period. The mean temperature has a regular cycle in all the observation stations, with the hottest months during austral summer (December to February) and the coldest months during austral winter (June to August). The summer (winter) mean monthly temperature ranges from 20.1 °C (5.1 °C) towards the south (Malargüe station) to 28.3 °C (12 °C) towards the north (La Rioja Aero station). The temperature amplitude between summer and winter is relatively small. The smallest amplitude (15.1 °C) was registered at Malargüe station, and the greatest at San Juan Aero station (18.7 °C).

The annual cycles of precipitation (Figure 3) concentrate peak values in the warm months and the lowest values in the cold months. The exception is the southwesternmost station with available data (Malargüe Aero), where precipitation peaks in autumn and winter, and reaches its lowest values in spring and summer. The annual cycle amplitude at Malargüe Aero is smaller than at the other stations and barely reaches 7% of the annual precipitation. In general, the annual cycle amplitude is below 20% of the total annual precipitation, except at Jachal, where it reaches 27%.

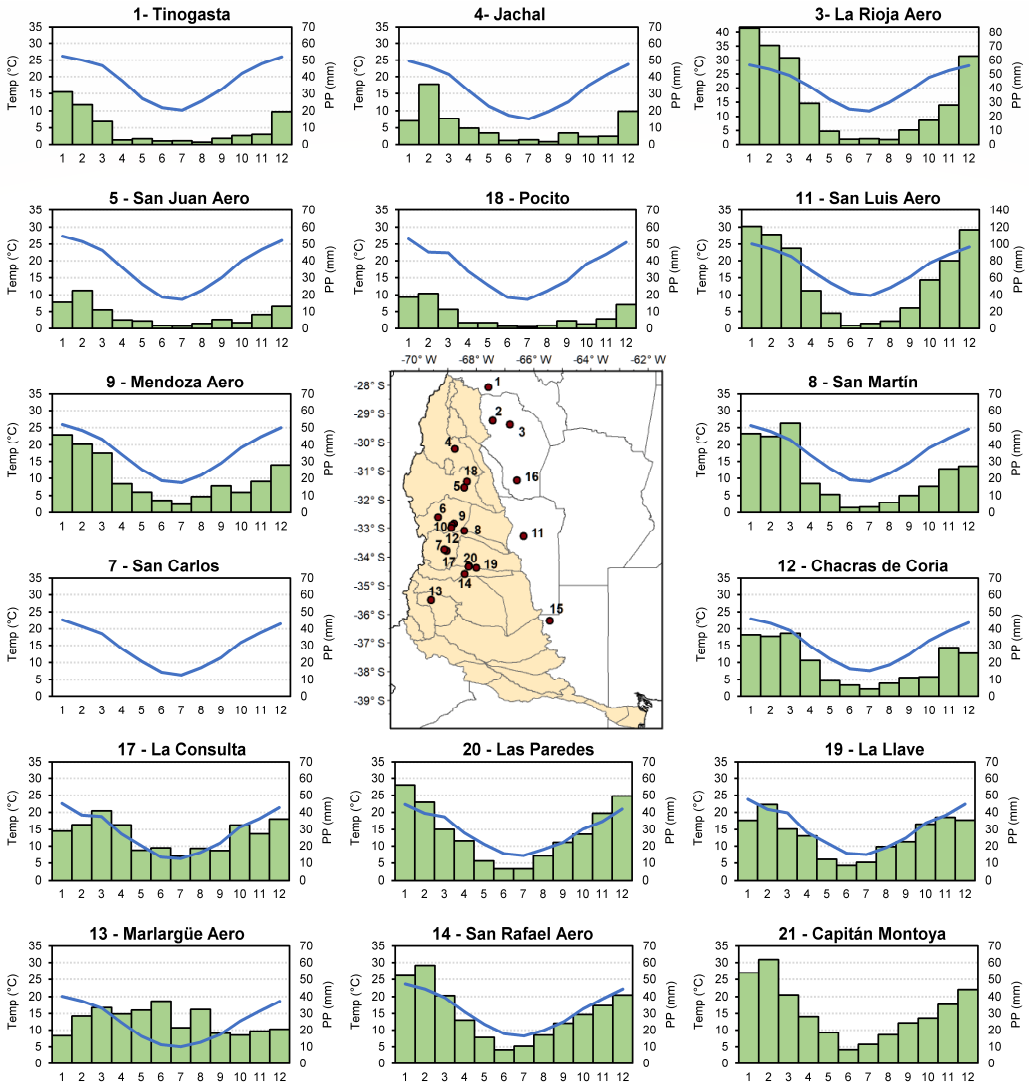

Figure 3. Annual cycles of mean monthly temperature (blue lines) and monthly precipitation (green bars). The map in the center shows the location of the stations. The temperature scale is the same in all panels (0–35 °C, **left** axis). The precipitation scale reaches 70 mm, except at La Rioja Aero, where it reaches 80 mm, and San Luis Aero, where it reaches 140 mm (**right** axis).

Monthly precipitation summer peaks vary markedly according to station location: they are smaller at the northwestern stations (Tinogasta, Jachal, San Juan Aero, and Pocito), and greater at the easternmost stations (e.g., La Rioja Aero and San Luis Aero). As discussed above, at the latter, precipitation amounts are well above those recorded at the remaining stations. Precipitation in Argentina is characterized by a westward decreasing gradient. San Luis Aero is located in a transition region, where precipitation decreases more rapidly towards the west. Therefore, all the stations located west of it present considerably lower values. On the other hand, the minimum monthly precipitation in winter amounts to a few millimeters; only La Consulta and Malargüe Aero have relatively higher values, close to 10 mm.

Figure 4 presents the annual cycles of the average SWE in the 1995–2014 period. SWE values begin to rise in winter and reach their peaks during the early spring, and then begin to decrease due to the temperature increase. Thus, as noted above, the precipitation (mainly in snow form) in the region presents a Mediterranean regime [29], with precipitation concentrated mostly during the cold season (April to October) and a dry warm season (November to March). The stations located in the north (Toscas and Laguna Diamante) reach SWE peaks between 200 and 400 mm at the end of the winter. The stations

located in the south (between –34.5°S and –6°S latitude) have SWE peaks between 800 and 1000 mm, also by the end of the winter. This snow is essential for water resource management in the central-western region of Argentina. Most of the rivers in the region are supplied by snowmelt in spring, the flow of which is used for irrigation and human consumption [11].

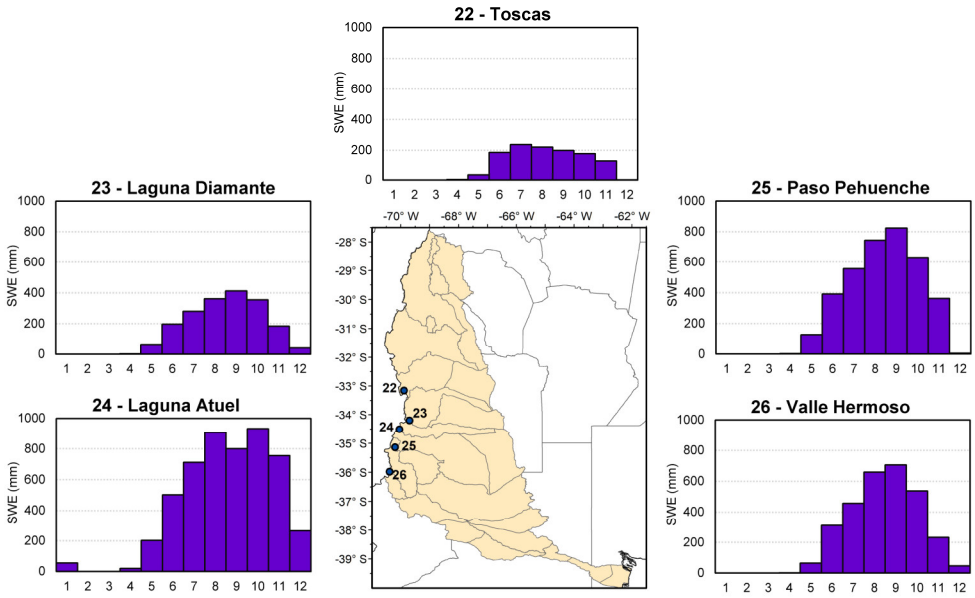

Figure 4. Annual cycles of SWE (mm) averaged over 1995–2014. The map shows the locations of the stations.

3.2. Variability and Changes

3.2.1. Temperature

Figure 5 shows the nonlinear trends at the nine selected stations for temperature. Those trends represent a major fraction of the total variance in the mean temperature series (between 56% and 20%; see Table A1). This result shows the relevance of long-period changes over interannual variability in the most recent decades. Consistent with world and regional warming [12,44], a noticeable increase in mean temperature is observed at most stations in the study region. At some stations, trends are more marked (Tinogasta, Mendoza Aero, San Carlos, Malargüe Aero, CA, USA), with sustained warming since 1961. The temperature rise is at least 1 °C from 1961 to 2020, and reaches 2 °C in Tinogasta, in the north of the study region, and in San Carlos, in the center-west. Other stations (Jachal, La Rioja Aero, San Juan Aero, San Luis Aero, Spain) do not show a clear signal of sustained warming according to the nonlinear trend patterns, but they are affected by decadal variability. However, in the most recent decades, trends are positive at all the stations. These results suggest that the region has experienced major positive changes in mean temperature, with great spatial variability in the distribution of those changes.

Regarding temporal interannual variability, Table A1 shows dominant modes with frequencies of 8.5 years and close to 3 years. These two variability bands account for important rates of mean temperature interannual variability. Our results indicate that besides the shift to warmer conditions in recent decades, mean temperature is greatly affected by interannual variability in different timescales.

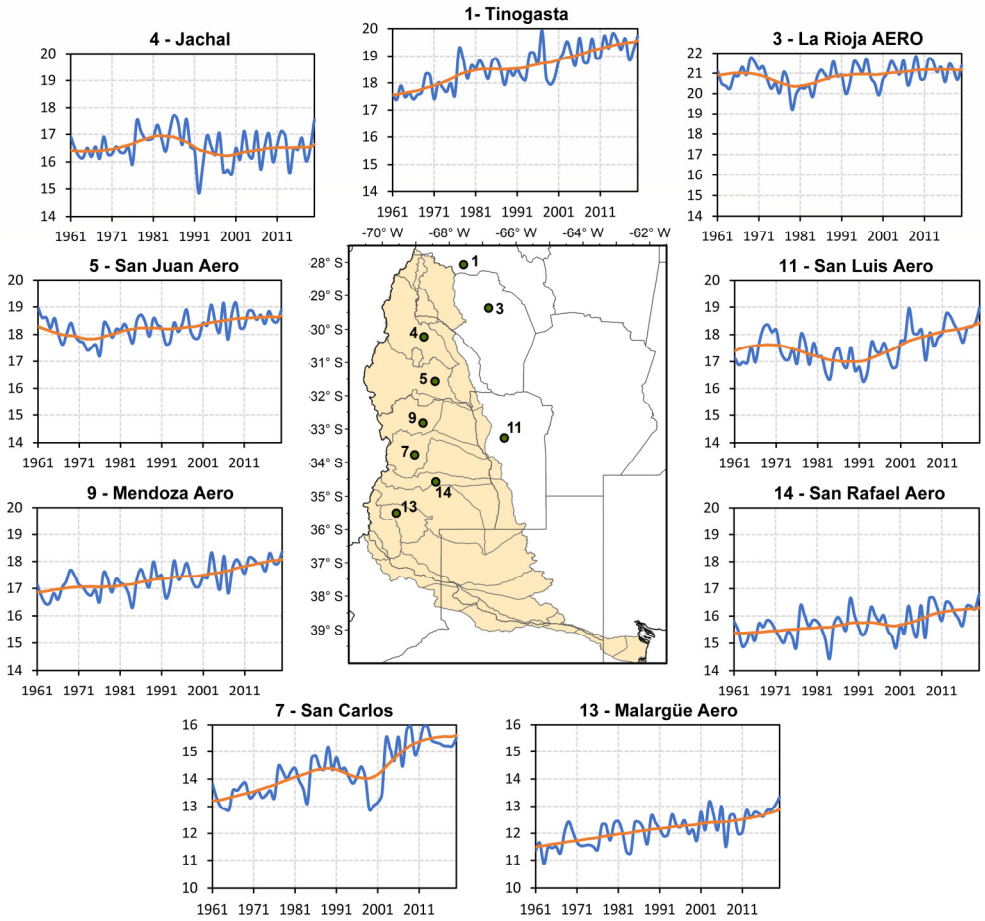

Figure 5. Mean annual temperature time series and their nonlinear trends. The map shows the locations of the stations. The temperature scale ranges between 14 and 20 °C, except at La Rioja Aero, where it reaches 22 °C, and at San Carlos and Malargüe, where it varies between 10 and 16 °C.

3.2.2. Precipitation

Annual precipitation in the study region presents nonlinear trends of varied relevance (see Figure 6 and Table A2). In general, these trends show positive changes with annual precipitation rises in recent decades, although the positive trends are not maintained throughout the period. The nonlinearity of the trends makes it possible to assume significant influence from decadal variability. The greatest changes were recorded at San Martín, in the center of the study region, where annual precipitation increased from mean values close to 180 mm in the period of 1961–1990 to 264 mm in 1991–2020. A similar temporal evolution is shown at Mendoza station (Figure 6). Consistently, the trends at Mendoza Aero and San Martín stations are the dominating modes associated with the first T-PC (Table A2). The trends at the other stations, including the La Rioja Aero, San Juan Aero, Malargüe, and San Rafael stations, show significant nonlinearities, although they also present an increase at the beginning of the study period that stabilizes from the 1970s.

Figure 6 also shows the relevance of interannual precipitation variability. At all stations, interannual modes explain large percentages of the time series variance (Table A2). This feature is frequently observed for precipitation, as it presents a more marked temporal variability than temperature. In this case, the dominant modes present their main frequencies in two variability bands: from 7.5 to 10 years, close to decadal variability, and between 2.8 and 4 years. Thus, our results indicate that the increase in precipitation is consistent in the entire region, although precipitation is greatly affected by interannual variability.

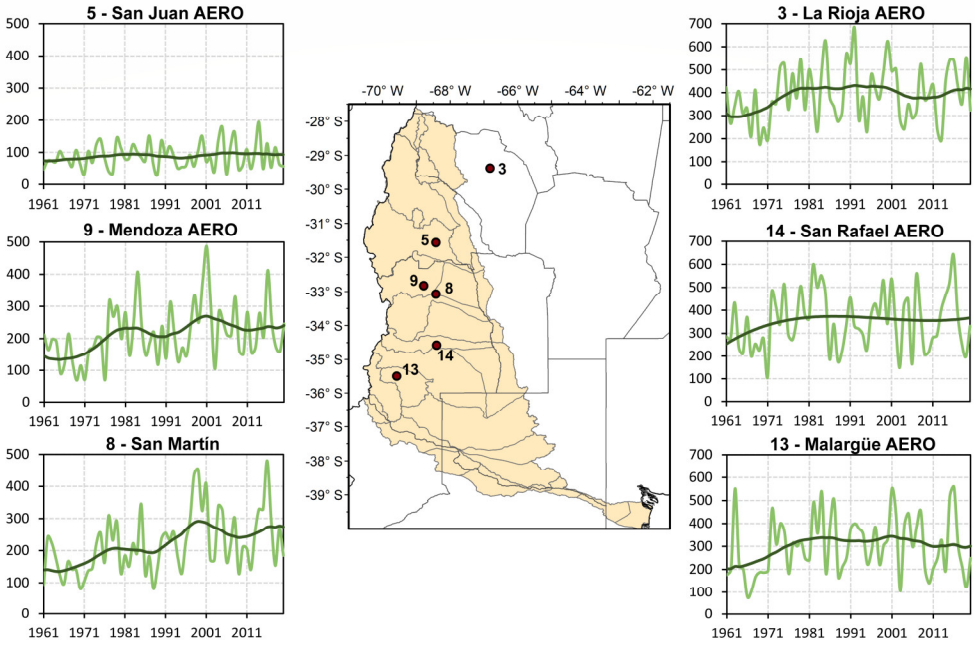

Figure 6. Annual precipitation time series at the six selected stations and their nonlinear trends. The map shows the locations of the stations. The precipitation scale reaches 500 mm at the drier stations (**left** column) and 700 at the wetter stations (**right** column).

3.2.3. Snow Water Equivalent

The available SWE data cover the 1990–2019 period, except at Paso Pehuenche station, where data are available between 1999 and 2019 (Table 1). Figure 7 presents the maximum annual SWE at each station. The interannual variability at all stations is large, and even more marked at some stations, such as Laguna Atuel. A marked decrease in SWE values is observed at all stations during the 2010s, while the previous decade includes years with high SWE at the five stations analyzed. The deficit in snowpacks impacted the main source of water for the rivers. Thus, the decreased snow propagated through the hydrological cycle components, leading to hydrological drought conditions in the adjacent foothills east of the Andes [11].

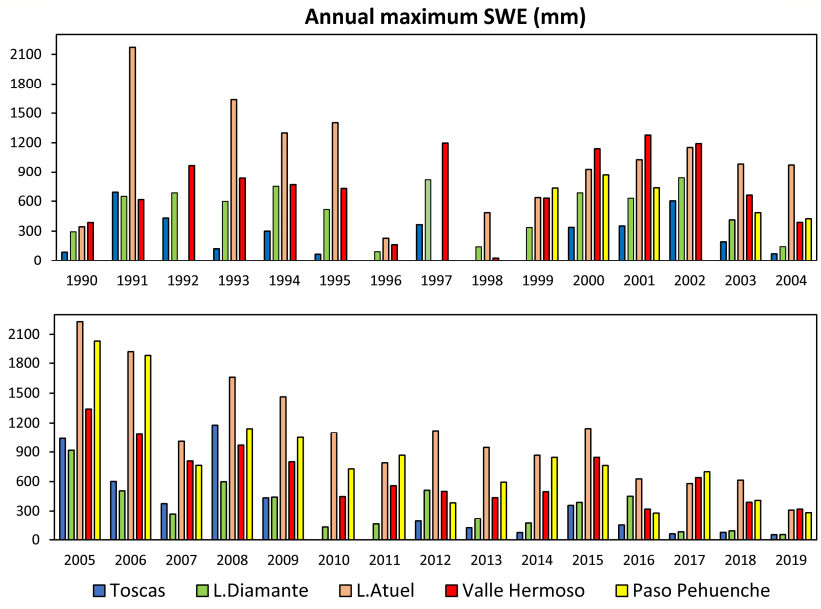

Figure 7. Annual maximum SWE (mm) in the 1990–2019 period.

3.3. Ability of the Models to Represent the Observed Variables

3.3.1. Temperature

Figure 8 presents Pearson´s correlations calculated between the monthly time series from the stations with long-term observations and the GCM ensemble and individual GCMs. Temperature is considerably well simulated in the study region, with correlation values between 0.90 and 0.98. Correlations differ slightly among the models and at each of the stations analyzed. The ensemble yields the best correlations—between 0.96 and 0.98—at most stations. The individual models HadGEM3-GC31-HM and CMCC-CM2-VHR4 (Figure 8d,e) have higher correlation values at most stations compared with EC-Earth3P-HR, CNRM-CM6-1-HR, and HiRAM-SIT-HR (Figure 8b,c,f). No marked spatial correlation pattern is observed in the study region.

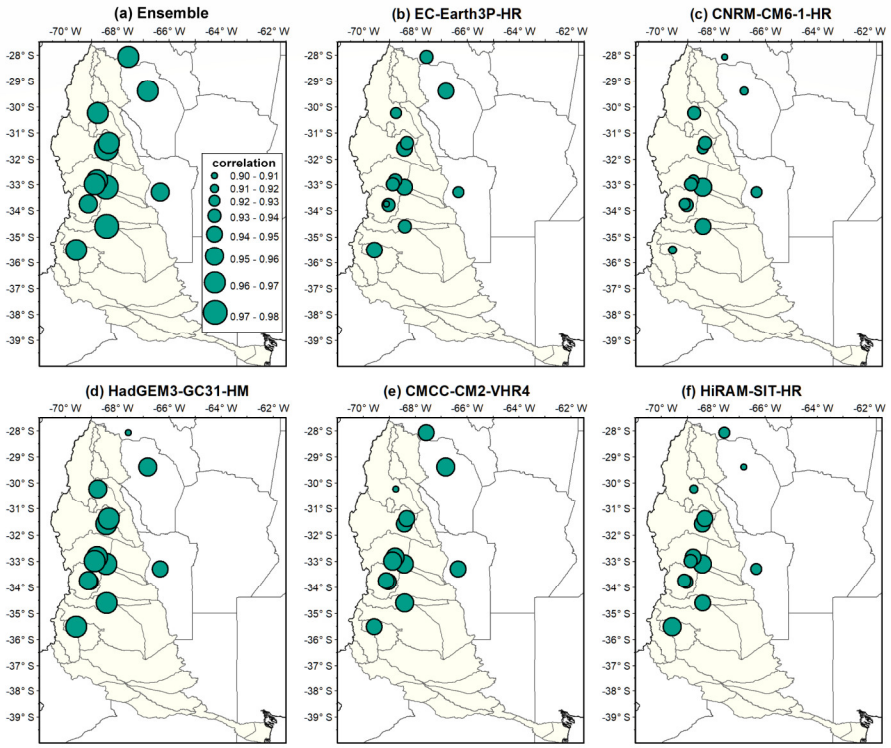

Figure 8. Pearson´s correlations between mean monthly temperature time series at the stations with long-term observations, and (**a**) GCM ensemble and (**b–f**) individual GCMs.

Figure 9 shows the mean bias error (MBE) of the monthly time series from the stations with long-term observations, the GCM ensemble, and the individual GCMs. In general, the models underestimate temperature observations at most stations, although the MBE varies according to the model and station. Some models only overestimate temperature at several stations (Figure 9e,f). On the other hand, although the ensemble presents underestimated values at all stations, MBE values are smaller in the ensemble than in individual models (Figure 9a).

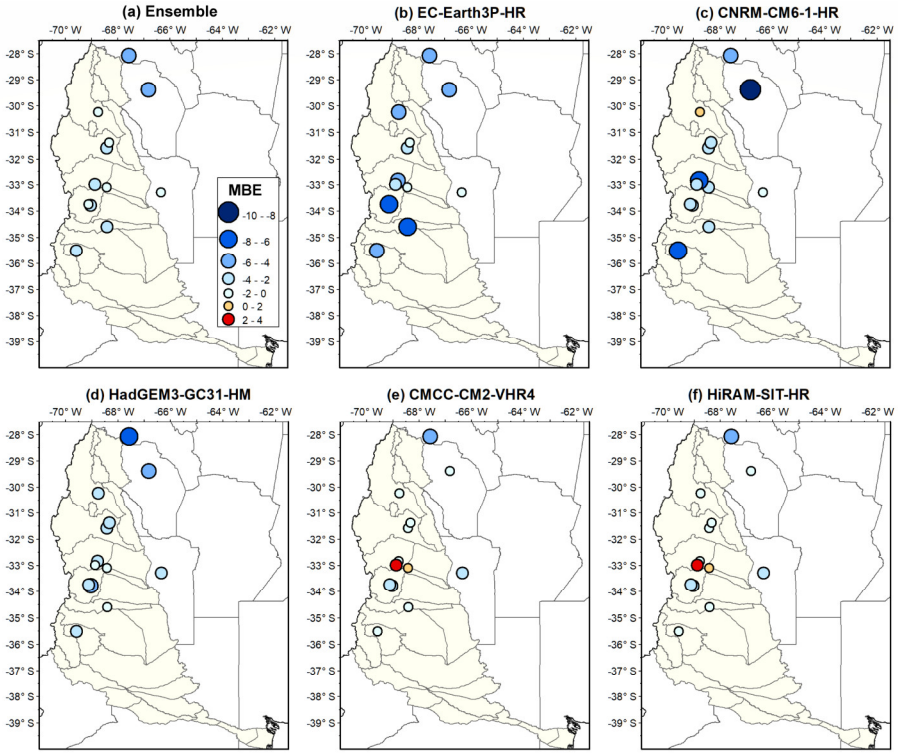

Figure 9. Mean bias error (MBE) values between mean monthly temperature time series from the stations with long-term observations and (**a**) GCM ensemble and (**b**–**f**) individual GCMs.

The root-mean-square error (RMSE) is shown in Figure 10 for the stations with long-term monthly observation, the GCM ensemble, and individual GCMs. The smallest RMSE at all the stations was obtained for the CMCC-CM2-VHR4 model (Figure 10e), followed by HiRAM-SIT-HR (Figure 10f) and the ensemble (Figure 10a). Note that the RMSE values at most of the stations range from 1–2 to 3–4 °C, which are very low error values for temperature. In general, the greatest RMSE occurs at the stations located in the north of the basin (6–7 °C), except for EC-Earth3P-HR (Figure 10b).

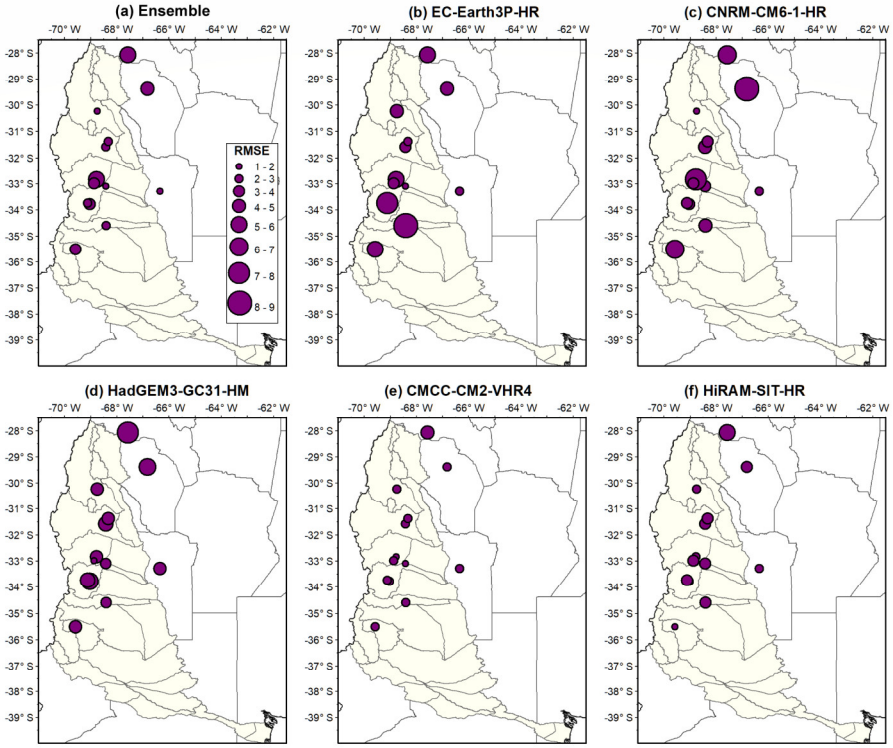

Figure 10. Root-mean-square error (RMSE) values between the mean monthly temperature time series at the stations with long-term records and (**a**) GCM ensemble and (**b**–**f**) individual GCMs.

3.3.2. Precipitation

Figure 11 presents Pearson´s correlations between the time series of monthly precipitation with long records of observations and the GCM ensemble and individual GCMs. For the study region, the correlations are positive in all the models (Figure 11b–f) and the ensemble (Figure 11a); i.e., there is a direct relationship between the simulations and observations in most of the cases. Nevertheless, the correlations are smaller (close to 0) at Malargüe Aero for the majority of the models. These features might be caused by the poor ability of the models to represent weather conditions in regions with complex topography or with singularities in the annual cycle (see Section 3.1). The ensemble (Figure 11a) presents the best correlations, with the highest values in the north (between 0.5 and 0.7). Again, the uncertainty in the model ensemble is smaller than those in the individual models, thus strengthening the efficiency of the simulations.

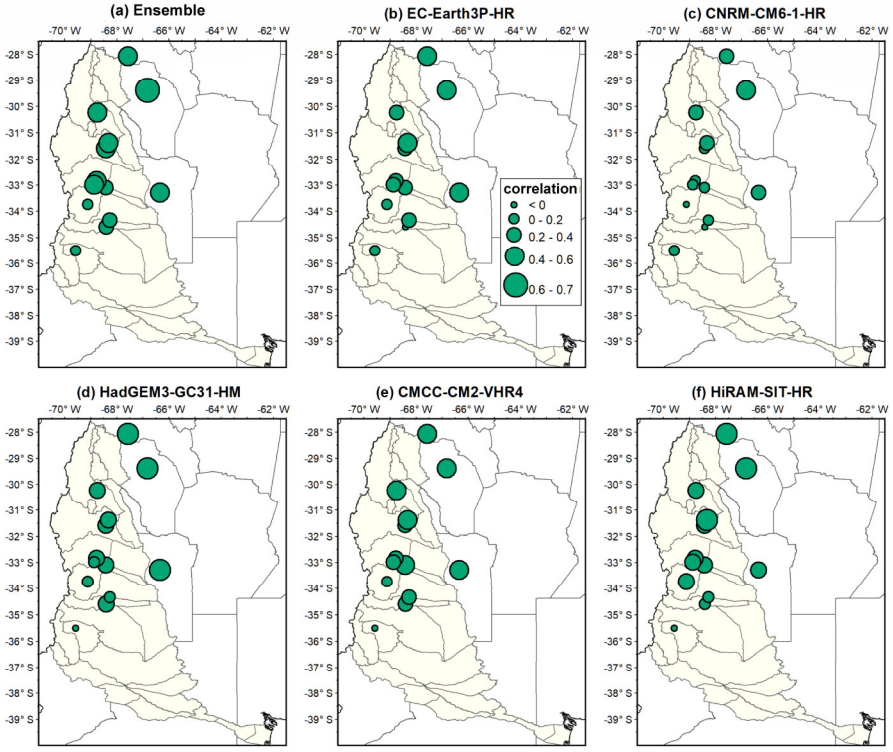

Figure 11. Pearson's correlation between the time series of monthly precipitation from stations with long-term records of observations and (**a**) the GCM ensemble and (**b**–**f**) individual GCMs.

Figure 12 shows the MBE values between the time series of monthly precipitation from stations with long-term records and the GCM ensemble and individual GCMs. The models are observed to overestimate precipitation at most of the stations under analysis, although the MBE values vary depending on the model and station (Figure 12b–f), which is also reflected in the values for the ensemble (Figure 12a). Some models, such as EC-Earth3P-HR and CNRM-CM6-1-HR (Figure 12b,c), overestimate the observations by over 100 mm, as observed at the San Carlos station. This overestimation is reflected in the ensemble (Figure 12a). However, the overestimations are smaller (0–20 mm) at certain stations. In particular, this range predominates at the stations simulated using HiRAM-SIT-HR (Figure 12f), which achieves the best fitting in terms of systematic errors, and even underestimates the observed precipitation by 0–20 mm at some stations in the south of the study region.

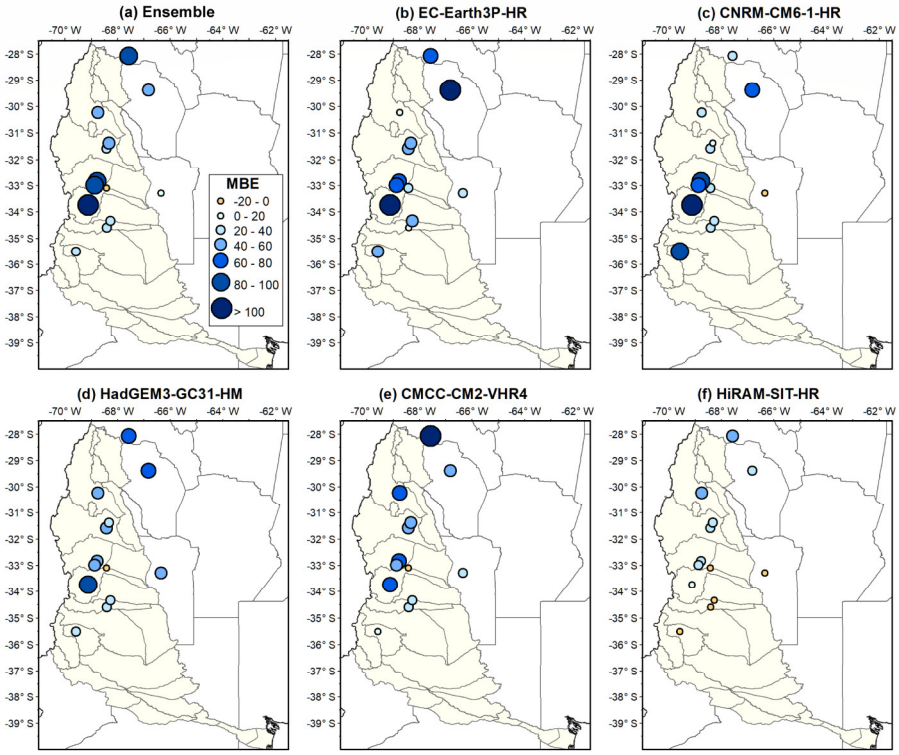

Figure 12. Mean bias error (MBE) values between monthly precipitation time series from stations with long-term observations and (**a**) the GCM ensemble and (**b**–**f**) individual GCMs.

Figure 13 presents the RMSE values between the monthly precipitation time series from stations with long-term observations and the GCM ensemble and individual GCMs. Given the poor ability of GCMs to represent regional precipitation at single stations, RMSE values are high for most of the models and the ensemble (Figure 13a). Lower RMSE values are obtained for the HiRAM-SIT-HR (Figure 13f) at most of the stations, except for those located in the north of the study region.

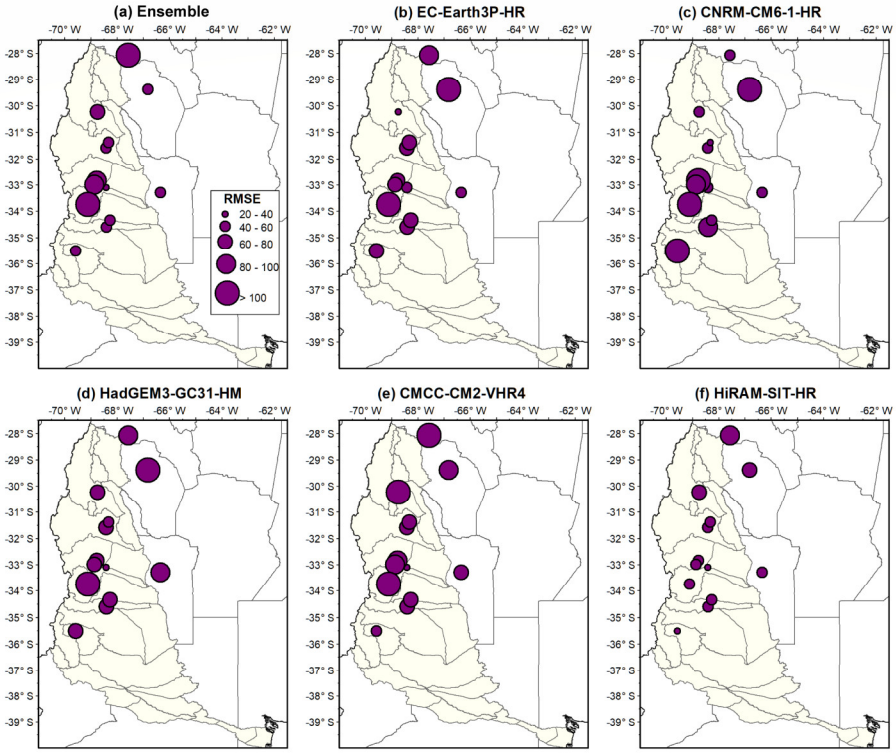

Figure 13. Root-mean-square error (RMSE) values between monthly precipitation time series from stations with long-term observations and (**a**) the GCM ensemble and (**b**–**f**) individual GCMs.

3.3.3. Snow Water Equivalent

The available data from five stations (the ones used in Section 3.2) have an acceptable length (1990–2019) for comparison with modeled data. The statistical metrics presented in Table 3 indicate that GCMs perform regularly in representing single SWE data, with low correlations and considerable mean bias errors (here presented as percentages). This was to be expected, given the great difficulty in modeling snow processes (even more than in the case of rainfall). In any case, the models are capable of recognizing the annual cycle of SWE, and although with systematic errors, they also recognize the monthly values at some stations (e.g., Valle Hermoso or Laguna Diamante). Better correlations are obtained from EC-Earth3P-HR than from CNRM-CM6-1-HR at all stations; the fit is also good with low MBE and RMSE values (except at Toscas station). Table 3 shows that EC-Earth3P-HR underestimates the SWE with MBE values between −12% and −2% (except at Toscas station). Consequently, with bias correction, the model is able to represent the SWE in the study region.

As an example, Figure 14 shows that the mean annual cycle and the monthly time series of SWE at Valle Hermoso station are poorly simulated by the CNRM-CM6-1-HR model, which overestimates the observed values with a high MBE (see also Table 3). After correcting this systematic error, the fits improve significantly and make it possible to obtain an annual cycle (Figure 14a) and a time series (Figure 14b) close to the observations (similar examples are shown for temperature and precipitation in Appendix B, Figures A1 and A2). A better fit is obtained for the bias-corrected simulations from the EC-Earth-3P-HR model than those from the CNRM-CM6-1-HR model, with values very similar to the observations. These results are also obtained for the other stations, except at Toscas station. Consequently, only the EC-Earth-3P-HR model is used for the analysis of future projections.

Table 3. SWE statistical metrics for the CNRM-CM6-1-HR and EC-Earth3P-HR models. MBE% indicates the percent mean bias error (see also Déqué 2010).

		CNRM-CM6-1-HR			
#	Station	MBE	MBE%	RMSE	r
1	Toscas	8008.5	8207.2	9557.3	0.049
2	Laguna Diamante	358.5	199.1	523.9	0.493
3	Laguna Atuel	7168.7	1581.4	7667.3	0.290
4	Paso Pehuenche	2850.9	936.1	3880.3	0.241
5	Valle Hermoso	734.0	287.1	1075.1	0.585
		EC-Earth3P-HR			
#	Station	MBE	MBE%	RMSE	r
1	Toscas	156.2	160.1	360.9	0.120
2	Laguna Diamante	−4.5	−2.5	223.9	0.537
3	Laguna Atuel	−54.5	−12.0	508.9	0.477
4	Paso Pehuenche	−8.4	−2.8	288.1	0.578
5	Valle Hermoso	−32.5	−12.7	254.0	0.710

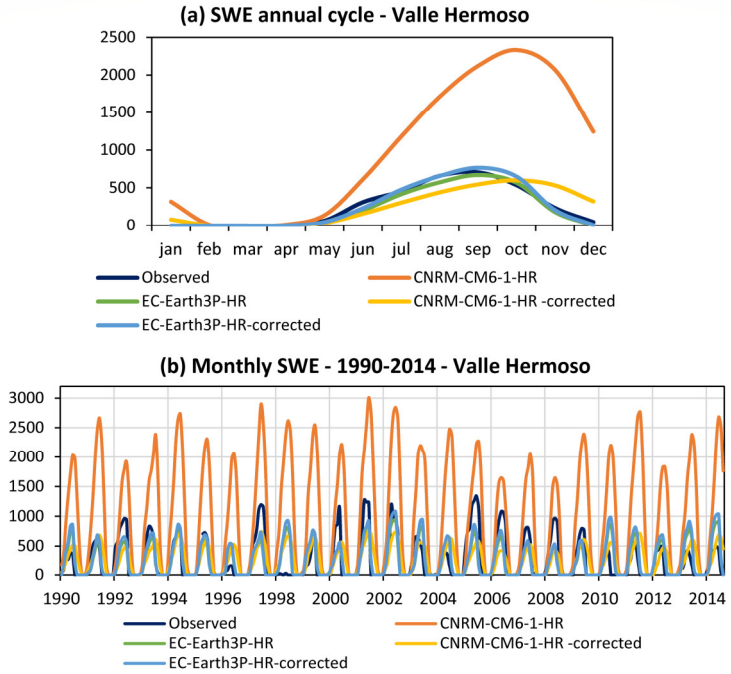

Figure 14. (**a**) Annual cycle (1995–2014) and (**b**) monthly time series (1990–2014) of SWE values (mm) observed at Valle Hermoso station and simulated by the models with and without bias correction.

3.4. Projected Changes

3.4.1. Temperature

Figure 15 presents the spatial distribution of the changes in mean annual temperature (°C) projected by the multi-model ensemble (Figure 15a) and individual models (Figure 15b–f). The ensemble has the advantage of reducing the uncertainty in both the internal variability in the climate system and in the models themselves [45], and its projections are more reliable. In this particular case, the ensemble projects a mean temperature rise over the entire region following an east–west gradient. In the center and the east of the study region, the warming is expected to be 1–1.5 °C in the 2021–2050 period. In the west, over the highest area of the Andes, the projected rise is between 1.5 and 2 °C. Finally, in the northernmost part of the study region, the warming might exceed 2°C. The spatial patterns of the individual models (Figure 15b–f), although with different variation ranges,

are consistent with the spatial pattern of the ensemble, which reinforces the reliability of the projections.

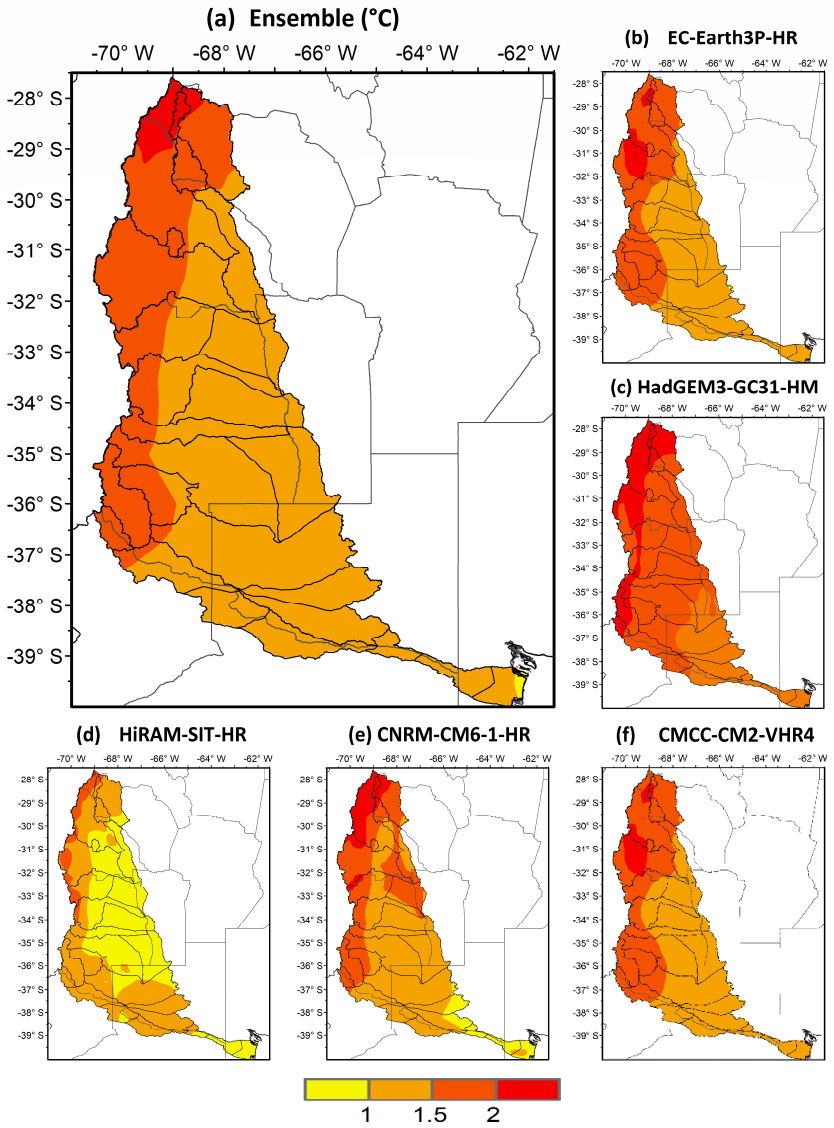

Figure 15. Spatial distribution of changes in mean annual temperature (°C) projected by (**a**) the multi-model ensemble (**b**–**f**) and individual models. Changes are computed between the 2021–2050 and 1985–2014 periods.

As an example, Figure 16 shows the temporal evolution of the observed mean annual temperature, the bias-corrected ensemble simulation of the historical period 1961–2014, and the bias-corrected ensemble simulation of the future period 2014–2050, with their respective intermodel ranges. In the historical period, the ensemble adequately reproduces observations, including the interannual variability and an upward temperature trend in recent decades. The trend remains positive in future decades, with an increase in annual temperature of up to 2° C in 2050 with respect to observation averaged over 1985–2014. The intermodel ranges are low and close to the ensemble simulations, which makes the projections of the mean temperature at La Rioja Aero have good certainty. Note also that the bias-correction method significantly improves the fit to the observations and enhances the overall reliability of the projections (see Appendix B).

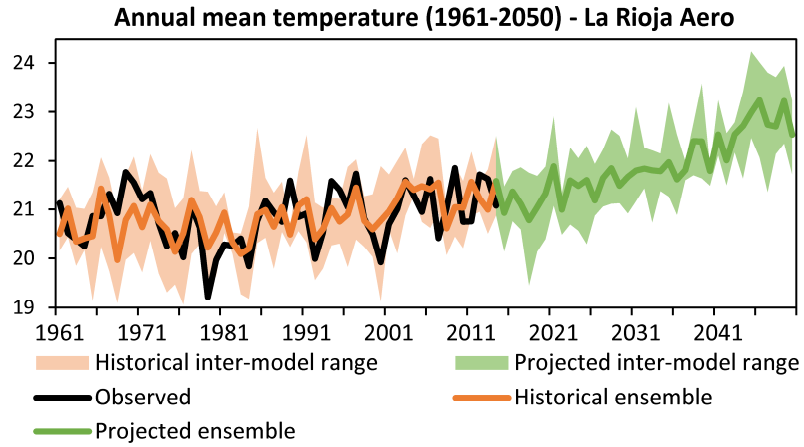

Figure 16. Observed simulation and bias-corrected ensemble projection of annual mean temperature (°C) at La Rioja Aero. Intermodel ranges of historical and future scenarios.

3.4.2. Precipitation

Figure 17 presents the spatial distribution of projected changes in annual precipitation according to the multi-model ensemble (Figure 17a) and the percentage above the mean values of the historical period (Figure 17b), and the individual models (Figure 17c–g). As is the case with temperature, the changes in precipitation also present an east–west gradient. In this case, the multi-model ensemble (Figure 17a) simulates an increase of up to 50 mm in the center-east of the study region. This change represents an increase of 0–5% in the center of the region and 5–10% in the east (Figure 17b). On the other hand, the simulations indicate a decrease in precipitation of 0–5% in the 2021–2050 period in the highest area in the Andes (the westernmost part of the study region). The greatest drop in annual precipitation would occur in the high mountains in the south of Mendoza (100 mm or more; Figure 17a). Unlike the changes in temperature, the spatial change patterns of the individual models (Figure 17c–h) are not consistent, although in general, they show a precipitation decrease in the east–west direction, as shown in the multi-model ensemble.

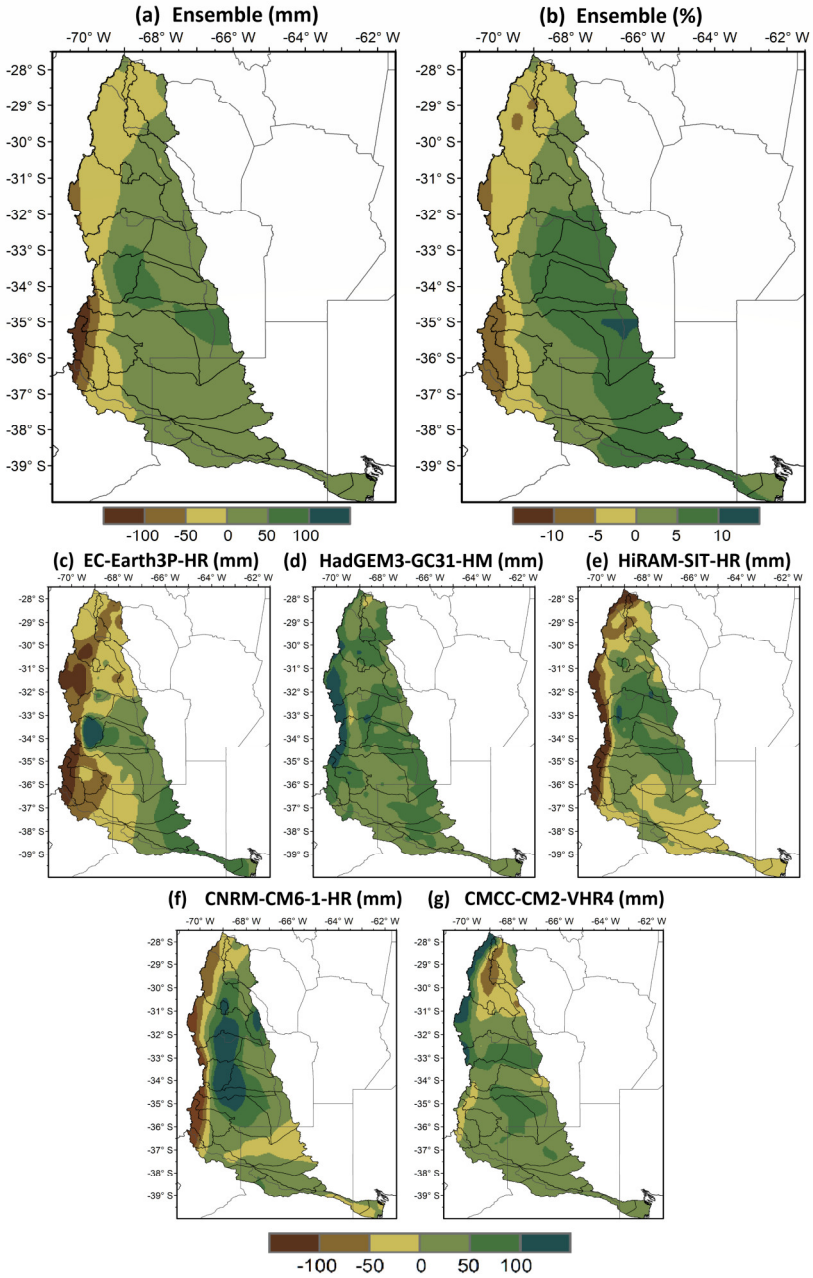

Figure 17. Spatial distribution of projected changes in annual precipitation (mm) according to (**a**) the multi-model ensemble, (**b**) the percentage exceeding mean values of the historical period, and (**c**–**g**) individual models.

Figure 18 shows the temporal evolution in annual precipitation, observed in the historical 1961–2014 period and simulated with the bias-corrected ensemble for the 2014–2050 period at La Rioja Aero. The ensemble reproduces the mean values of historical precipitation adequately, but it fails to reproduce the temporal variability. The bias-correction method allows a correct fitting to historical observations and the intermodel range is low, which indicates coherence among the simulations. No significant changes in annual precipitation are projected for this station.

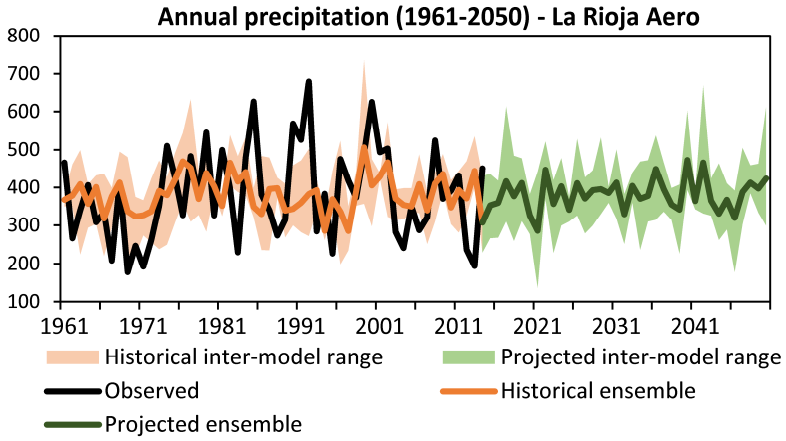

Figure 18. Observed and bias-corrected ensemble-simulated annual precipitation (mm) at La Rioja Aero. Historical and future intermodel ranges (shading).

3.4.3. Snow Water Equivalent

Figure 19 presents the spatial distribution of the mean annual and maximum annual SWE changes simulated with the high-resolution model that provides the best fit to the observations, namely the EC-Earth3p-HR model. The EC-Earth3p-HR model shows a projected decrease in mean annual and maximum annual SWE in the Andean regions, particularly in Mendoza between latitudes −34°S and −36°S, where most of the observations were registered. For that area, the model indicates that the maximum annual SWE decreases by between 100 and 150 mm in the 2021–2050 period (note that the model underestimates the observations by 10%), with peaks between 150 and 250 mm on the border with Chile (Figure 19b). The analysis of these results is limited by the uncertainty caused by the magnitude of the errors shown in Section 3.3.3 and by the fact that the simulations come from only one model. In any case, this decreasing trend has been noticed in previous years (as discussed in Section 3.2.3 and in [13]). Therefore, the projected decrease in SWE is consistent with the observations.

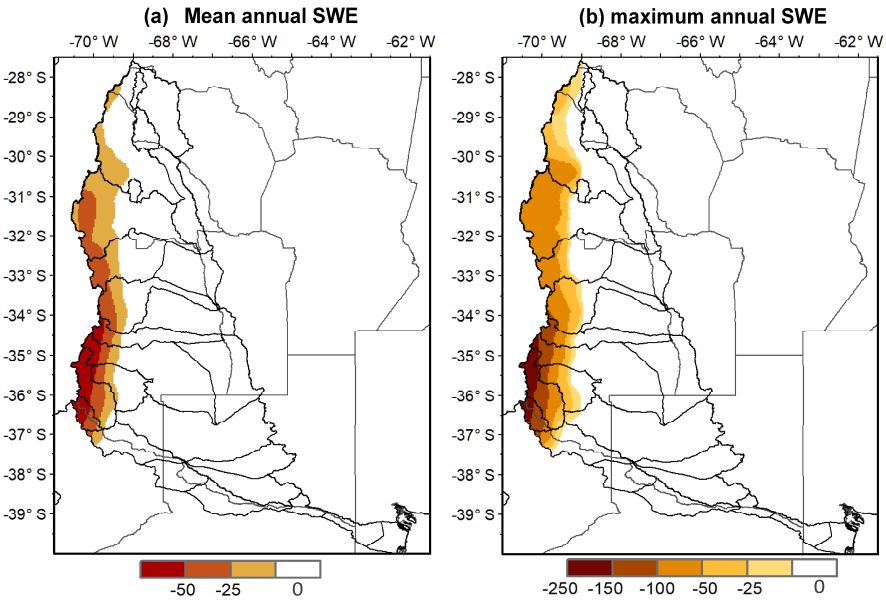

Figure 19. Spatial distribution of projected changes (mm) in (**a**) mean annual and (**b**) maximum annual SWE according to the model that best fits the observations (EC-Earth3p-HR) with respect to the values of the historical period (without bias correction).

To illustrate this statement, Figure 20 shows the monthly SWE observations at Valle Hermoso station and the monthly SWE simulated by the EC-Earth3p-HR model (with bias correction). In the case of the future simulations, the model shows a 27% reduction in SWE values for the 2021–2050 period. Figure 20 also shows that the temporal variability would remain, although there would be a considerable decrease in the frequency of winters with heavy snow, particularly after 2030. It is worth highlighting, as was pointed out previously, that the analysis of the results should take into account the limitations of models in representing snow processes, and the fact that we are using only one available model.

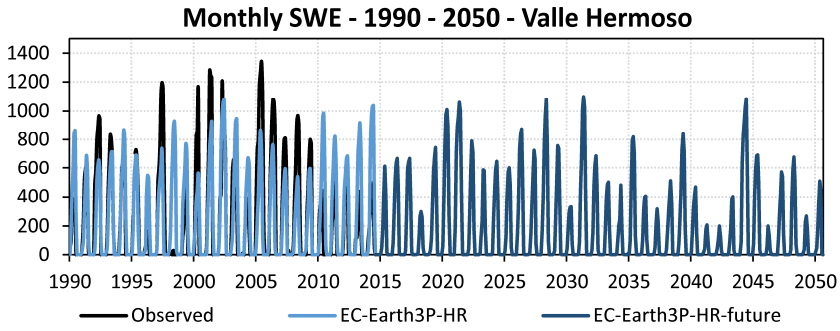

Figure 20. Observed and modeled monthly SWE time series at Valle Hermoso station. The model used is the one that best fits the observations (EC-Earth3p-HR), with bias corrections in the historical (1990–2014) and future (2015–2050) simulations.

4. Discussion and Conclusions

This study analyzes the mean conditions, the variability, and the changes in mean temperature, precipitation, and snow water equivalent in the Desaguadero-Salado-Chadileuvú-Curacó basin. The analysis covers a historical period (1961–2020) and a future period (2021–2050). In this study, we used a combination of observations, state-of-the-art high-resolution models to represent the regional climate, specifically the HighResMIP V1.0 simulations from the CMIP6 dataset, and robust statistical methods. The robustness of the results depends on the availability of enough high-quality observations, particularly when dealing with complex-topography regions as is the case with the Andes. The analysis of the present climate and the changes observed in a recent historical period was performed using the scarce observation series available in the region; therefore, our results are conditioned by the few existing observations.

The main hydrological processes in the DSCC basin are complex, mainly influenced by geographic and topographic factors, such as the altitude, slope, and aspect of the terrain. The mean temperature is around 12.5 °C in the higher areas in the west and 21 °C in the east and north of the basin. Annual rainfall decreases from east to west, with a large spatiotemporal variability. The annual cycle of rainfall presents a marked amplitude between the summer peaks and winter minima of a few millimeters towards the east of the Andes. The seasonality is more noticeable near the Andean foothills (see also [30]). Summer precipitation is dominated by convective rainfalls associated with moisture fluxes from the Amazon and Atlantic basins [46,47]. The snow water equivalent over the Andes begins to rise in winter, reaches its maximum value at the end of the winter and early spring (when the streamflow of the main river peaks), and decreases in summer, when it can equal zero. According to [15], the dry warm season from October to March responds to the seasonal displacement of the Southeastern Pacific High.

The study region has undergone a major warming in mean temperature, with increases of between 1 and 2 °C in recent decades. These temperature changes present large spatial variability. Annual precipitation has nonlinear trends of differing importance, which are generally positive. These results suggest there is increasing precipitation over the lowlands, east of the Andes. After 2005, the snow water equivalent decreased markedly in the Andes mountains in the province of Mendoza, which is where observations

are available. In addition, the mean temperature and precipitation present significant interannual variability modes, within two dominant variability bands: one between 7.5 and 10 years, and the other one, of higher frequency, between 2.8 and 4 years. The latter higher frequency cycles have been linked to El Niño–Southern Oscillation (ENSO)-like frequencies. The extreme phases of the ENSO phenomenon favor positive snow and rainfall anomalies (El Niño events) or may lead to water deficits (La Niña events) [26,48].

The studied HighResMIP models correctly simulated the mean temperature, reaching correlations in the range of 0.90–0.98. The multi-model ensemble improves the performance of the individual GCMs. The multi-model ensemble reaches correlations higher than 0.96. Regional precipitation features are reproduced with diverse degrees of success. Again, the multi-model ensemble achieves the best evaluation metrics, with correlations higher than 0.5 at most stations and lower MBE and RMSE values when compared with individual models. The SWE is simulated using high-resolution models with great difficulty. However, the applied bias-correction method substantially improves the historical simulation, favoring especially the analysis of snow and precipitation features over the study region.

Mean temperature is projected to rise in the entire study region, with growing values towards the west of the DSCC basin. Increments in the center and east of the study region are expected to be 1–1.5 °C in the period 2021–2050. The highest mountain area in the west would undergo a mean temperature rise between 1.5 and 2 °C. Finally, in the northernmost area of the study region, the increase might exceed 2 °C. The average annual precipitation in 2021–2050 is projected to exceed the 1985–2014 average by up to 50 mm over most of the basin, except in the westernmost area, where it is projected to decrease by 0–5%. The projected increase is about 0–5% of the precipitation in the central area and 5–10% in the east. A major drop would occur in the high mountains in the south of Mendoza. A decrease is expected in the maximum annual SWE in the Andes in the period 2021–2050; this decrease would be more marked towards the south of Mendoza. These results mark a continuation of recent trends.

Our results, which are consistent with those previously reported by [11,13,22], suggest that the management of scarce water resources in the basin should be made more efficient in the coming decades. The basin is an area with complex access to water, which has become even more complicated with the increase in temperatures and the lack of snow in recent decades. Our results indicate that these changes will be exacerbated in the next 30 years: temperatures will continue to rise and precipitation (rain and snow) will continue to decrease in the Andes mountains, particularly in Mendoza. On the other hand, the projected precipitation increases over the eastern portion of the DSCC basin will be beneficial for the growing development of regional agriculture. In this region, the main crops include grapes and olives on the plains near the Andes [49], while peanuts, maize, soybeans, and cattle raising are more relevant in the eastern portion [13]. These future scenarios raise the need to generate integrated water management plans that facilitate an efficient use of the resource. The access to water will be more difficult towards the Andes and, on the other hand, it will be favored by the increase in rainfall in the lowlands in the coming decades.

Author Contributions: Conceptualization, G.V.M. and M.A.L.; methodology, G.V.M. and M.A.L.; software, G.V.M. and M.A.L.; validation, G.V.M. and M.A.L.; formal analysis, G.V.M. and M.A.L.; investigation, G.V.M. and M.A.L.; resources, G.V.M. and M.A.L.; data curation, G.V.M. and M.A.L.; writing—original draft preparation, G.V.M. and M.A.L.; writing—review and editing, G.V.M. and M.A.L.; visualization, G.V.M. and M.A.L.; project administration, G.V.M. and M.A.L.; funding acquisition, G.V.M. and M.A.L. All authors have read and agreed to the published version of the manuscript.

Funding: This research was funded by the National Agency for Scientific and Technological Promotion of Argentina (project nos. PICT- 2019-2019-03982 and PICT-2019-2019-00481), the Universidad Nacional del Litoral (grant no. CAI+D- 2020-50620190100082LI), and the Argentine National Council for Scientific and Technical Research (grant no. PIP-CONICET 11220200102257CO). The

APC was funded by the National Agency for Scientific and Technological Promotion of Argentina (project nos. PICT- 2019-2019-03982).

Data Availability Statement: CMIP6 multi-model dataset is publicly available at https://esgf-node.llnl.gov/projects/cmip6/ (accessed on 28 April 2023). The SWE belong to the National Hydrological Network of Argentina and is publicly available at https://snih.hidricosargentina.gob.ar/ (accessed on 29 April 2023). Restrictions apply to the availability of observed meteorological station data. The temperature and precipitation data belong to the National Weather Service, National Institute of Agricultural Technology of Argentina, and the Directorate of Agriculture and Climatic Contingencies of Mendoza province (Argentina) and are available upon request from https://www.smn.gob.ar/ (accessed on 29 April 2023), https://www.argentina.gob.ar/inta (accessed on 29 April 2023), and https://www.mendoza.gov.ar/contingencias/ (accessed on 29 April 2023).

Acknowledgments: We are grateful to the anonymous reviewers who helped to improve the manuscript.

Conflicts of Interest: The authors declare no conflict of interest.

Appendix A

Table A1. Dominant modes identified with SSA for mean annual temperature time series.

Nº	Station	Components	Trend or Dominant Period (Years/Cycle)	Explained Variance (%)
1	Tinogasta	T-PC1	Trend	55.5
		T-PC2/T-PC3	8.5	14.8
		T-PC4/T-PC5	2.8	12.53
		T-PC3/T-PC4	2.6	28.2
2	La Rioja	T-PC1	Trend	25.6
		T-PC2/T-PC3	8.5	30
		T-PC4/T-PC5	2.8	16.6
3	Jachal	T-PC1	Trend	19.4
		T-PC2/T-PC3	8.5	25.5
		T-PC4/T-PC5	3.74	20.4
4	San Juan Aero	T-PC1	Trend	33.7
		T-PC2/T-PC3	2.85	18.2
		T-PC4/T-PC5	4	16.14
5	San Carlos	T-PC1	Trend	59
		T-PC2/T-PC3	8.5	19.5
		T-PC4/T-PC5	2.8	9.35
6	Mendoza Aero	T-PC1	Trend	37.3
		T-PC2/T-PC3	8.5	20.7
		T-PC4/T-PC5	2.8	16.4
7	San Luis Aero	T-PC1	Trend	41.8
		T-PC2/T-PC3	8.5	31.2
		T-PC4/T-PC5	2.3	9.3
8	Malargüe	T-PC1	Trend	36.8
		T-PC2/T-PC3	4	20.2
		T-PC4/T-PC5	8.5	16.3
9	San Rafael	T-PC1	Trend	24
		T-PC2/T-PC3	8.5	28.7
		T-PC4/T-PC5	4	17.8

Table A2. Dominant modes identified with SSA for annual precipitation time series.

Nº	Station	Components	Trend or Dominant Period (Years/Cycle)	Explained Variance (%)
1	La Rioja	T-PC1 y T-PC2	8.5	35.5
		T-PC3	Trend	12.6
2	San Juan Aero	T-PC1 y T-PC2	3	34
		T-PC3 y T-PC4	4.2	26.4
		T-PC5 y T-PC6	6	19.5
		T-PC9	Trend	3.5
3	San Martin	T-PC1	Trend	28.4
		T-PC2 y T-PC3	7.5	32.3
		T-PC4 y T-PC5	2.8	17.9
4	Mendoza Aero	T-PC1	Trend	22.6
		T-PC3 y T-PC4	3.3	24.3
5	Malargüe	T-PC1 y T-PC2	10	35.8
		T-PC3 y T-PC4	3.5	24.2
		T-PC8	Trend	7.3
6	San Rafael	T-PC1 y T-PC2	8.5	36.0
		T-PC3 y T-PC4	2.6	25.8
		T-PC5	Trend	11.2

Appendix B

Bias correction makes it possible to improve the results of simulations. As an example, Figure A1 shows the annual cycle of the mean monthly temperature (Figure A1a) and the mean annual temperature time series of the observed data and multi-model ensemble with and without bias correction at La Rioja Aero (Figure A1b). Both figures show that bias correction improves the simulation results considerably. The annual cycle, though underestimated (MBE = −4.5 °C), is clearly well represented by the ensemble (Figure A1a). The local scaling removes the MBE, favoring the fitting. The RMSE drops from 4.8 °C to 1.2 °C. Therefore, the corrected ensemble has the ability to adequately represent the observed mean monthly temperature. Moreover, the corrected ensemble is able to represent the temporal evolution of the mean annual temperature and its interannual variability (Figure A1b).

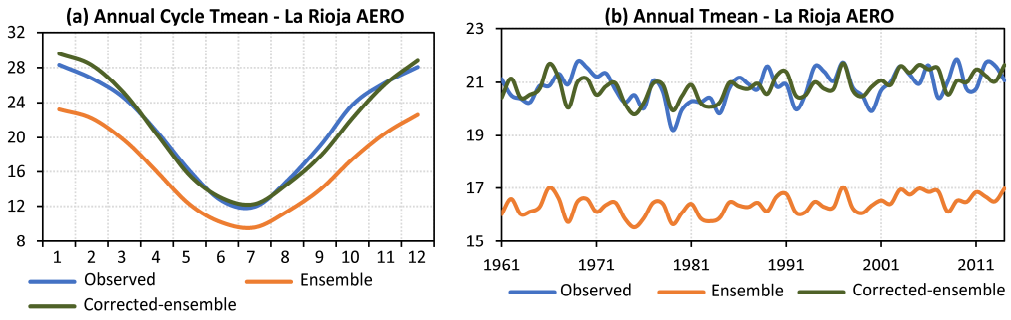

Figure A1. (**a**) Annual cycle of mean monthly temperature (°C) and (**b**) time series of mean annual temperature (°C) observed at La Rioja Aero and simulated using the multi-model ensemble with and without bias correction.

Figure A2 presents the observed and bias-corrected and noncorrected ensemble simulations of the annual cycle of monthly precipitation and annual precipitation at La Rioja Aero. The model ensemble adequately reproduces the annual cycle, although it

overestimates precipitation amounts considerably (MBE = 41 mm). Bias correction introduces a significant improvement to the fitting, reducing the RMSE from 59 mm to 32 mm and providing a good fitting for the annual cycle (Figure A2a). The corrected ensemble simulation also reproduces the temporal evolution of annual precipitation correctly, but fails to reproduce interannual variability (Figure A2b).

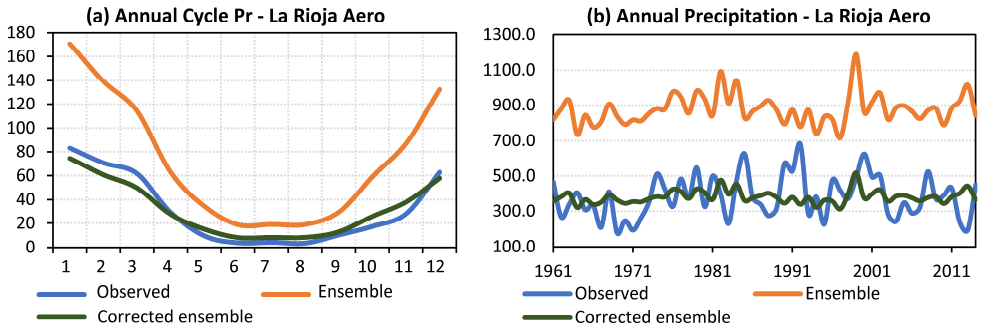

Figure A2. Observed and ensemble simulations (with and without bias correction) at La Rioja Aero; (**a**) annual cycle of monthly precipitation (mm) and (**b**) annual precipitation (mm).

References

1. Cai, W.; Cowan, T.; Thatcher, M. Rainfall reductions over Southern hemisphere semi-arid regions: The role of subtropical dry zone expansion. *Sci. Rep.* **2012**, *2*, 702. https://doi.org/10.1038/srep00702.
2. Sgroi, L.C.; Lovino, M.; Berbery, E.H.; Müller, G.V. Characteristics of droughts in Argentina's Core Crop Region. *Hydrol. Earth Syst. Sci.* **2020**, *25*, 2475–2490. https://doi.org/10.5194/hess-25-2475-2021.
3. Carril, A.F.; Cavalcanti, I.F.A.; Menéndez, C.G.; Sörensson, A.; López-Franca, N.; Rivera, J.; Robledo, F.; Zaninelli, P.; Ambrizzi, T.; Penalba, O.; et al. Extreme events in the La Plata basin: A retrospective analysis of what we have learned during CLARIS-LPB project. *Clim. Res.* **2015**, *68*, 95–116. https://doi.org/10.3354/cr01374.
4. Avila-Diaz, A.; Benezoli, V.; Justino, F.; Torres, R.; Wilson, A. Assessing current and future trends of climate extremes across Brazil based on reanalyses and earth system model projections. *Clim. Dyn.* **2020**, *55*, 1403–1426. https://doi.org/10.1007/s00382-020-05333-z.
5. Boisier, J.P.; Rondanelli, R.; Garreaud, R.D.; Muñoz, F. Anthropogenic and natural contributions to the Southeast Pacific precipitation decline and recent megadrought in central Chile. *Geophys. Res. Lett.* **2016**, *43*, 413–421. https://doi.org/10.1002/2015GL067265.
6. Garreaud, R.D.; Alvarez-Garreton, C.; Barichivich, J.; Boisier, J.P.; Christie, D.; Galleguillos, M.; LeQuesne, C.; McPhee, J.; Zambrano-Bigiarini, M. The 2010–2015 megadrought in central Chile: Impacts on regional hydroclimate and vegetation. *Hydrol. Earth Syst. Sci.* **2017**, *21*, 6307–6327. https://doi.org/10.5194/hess-21-6307-2017.
7. Skansi, M.; Brunet, M.; Sigró, J.; Aguilar, E.; Arevalo Groening, J.; Bentancur, O.; Castellón Geier, Y.; Correa Amaya, R.; Jácome, H.; Malheiros Ramos, A.; et al. Warming and wetting signals emerging from analysis of changes in climate extreme indices over South America. *Glob. Planet. Chang.* **2013**, *100*, 295–307. https://doi.org/10.1016/j.gloplacha.2012.11.004.
8. Lovino, M.; Müller, O.; Berbery, E.H.; Müller, G.V. How have daily climate extremes changed in the recent past over northeastern Argentina? *Glob. Planet. Chang.* **2018**, *168*, 78–97. https://doi.org/10.1016/j.gloplacha.2018.06.008.
9. Cerón, W.L.; Kayano, M.T.; Andreoli, R.V.; Avila-Diaz, A.; Rivera, I.A.; Freitas, E.D.; Martins, J.A.; Souza, R.A.F. Recent intensification of extreme precipitation events in the La Plata Basin in southern South America (1981–2018). *Atmos. Res.* **2021**, *249*, 105299. https://doi.org/10.1016/j.atmosres.2020.105299.
10. Donnelly, C.; Greuell, W.; Andersson, J.; Gerten, D.; Pisacane, G.; Roudier, P.; Ludwig, F. Impacts of climate change on European hydrology at 1.5, 2 and 3 degrees mean global warming above preindustrial level. *Clim. Change* **2017**, *143*, 13–26. https://doi.org/10.1007/s10584-017-1971-7.
11. Rivera, J.A.; Otta, S.; Lauro, C.; Zazulie, N. A Decade of Hydrological Drought in Central-Western Argentina. *Front. Water* **2021**, *3*, 640544. https://doi.org/10.3389/frwa.2021.640544.
12. Barros, V.; Boninsegna, J.; Camilloni, I.; Chidiak, M.; Magrín, G.; Rusticucci, M. Climate change in Argentina: Trends, projections, impacts and adaptation. *Wiley Interdiscip. Rev. Clim. Chang.* **2015**, *6*, 151–169. https://doi.org/10.1002/wcc.316.
13. Rivera, J.A.; Naranjo Tamayo, E.; Viale, M. Water Resources Change in Central-Western Argentina Under the Paris Agreement Warming Targets. *Front. Clim.* **2020**, *2*, 587126. https://doi.org/10.3389/fclim.2020.587126.
14. Masiokas, M.H.; Rabatel, A.; Rivera, A.; Ruiz, L.; Pitte, P.; Ceballos, J.L.; Barcaza, G.; Soruco, A.; Bown, F.; Berthier, E.; et al. A review of the current state and recent changes of the Andean cryosphere. *Front. Earth Sci.* **2020**, *8*, 99. https://doi.org/10.3389/feart.2020.00099.

15. Rivera, J.A.; Penalba, O.C.; Villalba, R.; Araneo, D.C. Spatio-temporal patterns of the 2010-2015 extreme hydrological drought across the Central Andes, Argentina. *Water* **2017**, *9*, 652. https://doi.org/10.3390/w9090652.
16. Zazulie, N.; Rusticucci, M.; Raga, G.B. Regional climate of the Subtropical Central Andes using high-resolution CMIP5 models. Part II: Future projections for the twenty-first century. *Clim. Dyn.* **2018**, *51*, 2913–2925. https://doi.org/10.1007/s00382-017-4056-4.
17. Pabón-Caicedo, J.D.; Arias, P.A.; Carril, A.F.; Espinoza, J.C.; Borrel, L.F.; Goubanova, K.; Lavado-Casimiro, W.; Masiokas, M.; Solman, S.; Villalba, R. Observed and Projected Hydroclimate Changes in the Andes. *Front. Earth Sci.* **2020**, *8*, 61. https://doi.org/10.3389/feart.2020.00061.
18. Spinoni, J.; Barbosa, P.; Bucchignani, E.; Cassano, J.; Cavazos, T.; Christensen, J.H.; Christensen, O.B.; Coppola, E.; Evans, J.; Geyer, B.; et al. Future Global Meteorological Drought Hot Spots: A Study Based on CORDEX Data. *J. Clim*. **2020**, *33*, 3635–3661. https://doi.org/10.1175/JCLI-D-19-0084.1.
19. Almazroui, M.; Ashfaq, M.; Islam, M.N.; Kamil, S.; Abid, M.A.; O'Brien, E.; Ismail, M.; Reboita, M.S.; Sörensson, A.A.; Arias, P.A.; et al. Assessment of CMIP6 performance and projected temperature and precipitation changes over South America. *Earth Syst. Environ.* **2021**, *5*, 155–183. https://doi.org/10.1007/s41748-021-00233-6.
20. Hock, R.; Bliss, A.; Marzeion, B.; Giesen, R.H.; Hirabayashi, Y.; HUSS, M.; Radic, V.; Slangen, A.B.A. GlacierMIP–A model intercomparison of global-scale glacier mass-balance models and projections. *J. Glaciol.* **2019**, *65*, 453–467. https://doi.org/10.1017/jog.2019.22.
21. Arias, P.A.; Garreaud, R.; Poveda, G.; Espinoza, J.C.; Molina-Carpio, J.; Masiokas, M.; Viale, M.; Scaff, L.; van Oevelen, P.J. Hydroclimate of the Andes part II: Hydroclimate variability and sub-continental patterns. *Front. Earth Sci.* **2021**, *8*, 505467. https://doi.org/10.3389/feart.2020.505467.
22. Rivera, J.A.; Arnould, G. Evaluation of the ability of CMIP6 models to simulate precipitation over Southwestern South America: Climatic features and long-term trends (1901–2014). *Atmos. Res.* **2020**, *241*, 104953. https://doi.org/10.1016/j.atmosres.2020.104953.
23. Mindlin, J.; Shepherd, T.G.; Vera, C.S.; Osman, M.; Zappa, G.; Lee, R.W.; Hodges, K.I. Storyline description of Southern hemisphere midlatitude circulation and precipitation response to greenhouse gas forcing. *Clim. Dyn.* **2020**, *54*, 4399–4421. https://doi.org/10.1007/s00382-020-05234-1.
24. Villamayor, J.; Khodri, M.; Villalba, R.; Valérie Daux. Causes of the long-term variability of southwestern South America precipitation in the IPSL-CM6A-LR model. *Clim. Dyn.* **2021**, *57*, 2391–2414. https://doi.org/10.1007/s00382-021-05811-y.
25. Rivera, J.A.; Araneo, D.C.; Penalba, O.C. Threshold level approach for streamflow droughts analysis in the Central Andes of Argentina: A climatological assessment. *Hydrol. Sci. J.* **2017**, *62*, 1949–1964. https://doi.org/10.1080/02626667.2017.1367095.
26. Berri, G.J.; Bianchi, E.; Müller, G.V. El Niño and La Niña influence on mean river flows of southern South America along the twentieth century. *Hydrol. Sci. J.* **2019**, *64*, 900–909. https://doi.org/10.1080/02626667.2019.1609681.
27. Lauro, C.; Vich, A.I.; Moreiras, S.M. Streamflow variability and its relationship with climate indices in western rivers of Argentina. *Hydrol. Sci. J.* **2019**, *64*, 607–619. https://doi.org/10.1080/02626667.2019.1594820.
28. Bereciartua, P.; Antunez, N.; Manzelli, L.; López, P.; Callau Poduje, A.C. Estudio Integral de la Cuenca del Río Desaguadero-Salado-Chadileuvú-Curacó. Subsecretaría de Recursos Hídricos de la Nación—Universidad de Buenos Aires 2009. Available online: https://cuencadesaguadero.weebly.com/biblioteca.html (accessed on 2 March 2023).
29. Viale, M.; Nuñez, M.N. Climatology of winter orographic precipitation over the subtropical central Andes and associated synoptic and regional characteristics. *J. Hydrometeorol.* **2011**, *12*, 481–507. https://doi.org/10.1175/2010JHM1284.1.
30. Doyle, M.E. Observed and simulated changes in precipitation seasonality in Argentina. *Int. J. Climatol.* **2020**, *40*, 1716–1737. https://doi.org/10.1002/joc.6297.
31. Viale, M.; Bianchi, E.; Cara, L.; Ruiz, L.E.; Villalba, R.; Pitte, P.; Masiokas, M.; Rivera, J.; Zalazar, L. Contrasting climates at both sides of the Andes in Argentina and Chile. *Front. Earth Sci.* **2019**, *7*, 69. https://doi.org/10.3389/fenvs.2019.00069.
32. World Meteorological Organization (WMO). *WMO Guidelines on the Calculation of Climate Normals. WMO-No. 1203*; WMO: Geneva, Switzerland; p. 29. Available online: https://library.wmo.int/doc_num.php?explnum_id=4166 (accessed on 21 April 2023).
33. Masiokas, M.; Villalba, R.; Luckman, B.; Le Quesne, C.; Aravena, J.C. Snowpack variations in the Central Andes of Argentina and Chile, 1951–2005: Large-scale atmospheric influences and implications for water resources in the region. *J. Clim.* **2006**, *19*, 6334–6352. https://doi.org/10.1175/JCLI3969.1.
34. Haarsma, R.J.; Roberts, M.J.; Vidale, P.L.; Senior, C.A.; Bellucci, A.; Bao, Q.; Bao, Q.; Chang, P.; Corti, S.; Fučkar, N.S.; et al. High Resolution Model Intercomparison Project (HighResMIP v1.0) for CMIP6. *Geosci. Model Dev.* **2016**, *9*, 4185–4208. https://doi.org/10.5194/gmd-9-4185-2016.
35. Eyring, V.; Bony, S.; Meehl, G.A.; Senior, C.A.; Stevens, B.; Stouffer, R.J.; Taylor, K.E. Overview of the coupled model intercomparison project phase 6 (CMIP6) experimental design and organization. *Geosci. Model. Dev.* **2016**, *9*, 1937–1958. https://doi.org/10.5194/gmd-9-1937-2016.
36. Zazulie, N.; Rusticucci, M.; Raga, G.B. Regional climate of the subtropical Central Andes using high resolution CMIP5 models. Part I: Past performance (1980–2005). *Clim. Dyn.* **2017**, *49*, 3937–3957. https://doi.org/10.1007/s00382-017-3560-x.
37. Ghil, M.; Allen, M.; Dettinger, M.; Ide, K.; Kondrashov, D.; Mann, M.; Robertson, A.; Saunders, A.; Tian, Y.; Varadi, F.; et al. Advanced spectral methods for climatic time series. *Rev. Geophys.* **2002**, *40*, 3–1–3–41. https://doi.org/10.1029/2000RG000092.

38. Wilks, D.S. *Statistical Methods in the Atmospheric Sciences*, 2nd ed.; Academic Press: Cambridge, MA, USA, 2006; p. 627.
39. Ghil, M.; Vautard, R. Interdecadal oscillations and the warming trend in global temperature time series. *Nature* **1991**, *350*, 324–327. https://doi.org/10.1038/350324a0.
40. Vautard, R. Patterns in Time: SSA and MSSA. In *Analysis of Climate Variability*; Von Storch, H., Navarra, A., Eds.; Springer: Berlin/Heidelberg, Germany, 1999; pp. 265–286. https://doi.org/10.1007/978-3-662-03744-7_14.
41. Allen, M.R.; Smith, L.A. Monte Carlo SSA: Detecting irregular oscillations in the presence of colored noise. *J. Clim.* **1996**, *9*, 3373–3404. https://doi.org/10.1175/1520-0442(1996)009<3373:MCSDIO>2.0.CO;2.
42. Déqué, M. Continuous variables. In *Forecast Verification—a Practitioner's Guide in Atmospheric Science*, 2nd ed.; Jolliffe, I.T., Stephenson, D.V., Eds.; John Wiley and Sons: Hoboken, NJ, USA, 2012; pp. 97–120.
43. Maraun, D.; Wetterhall, F.; Ireson, A.; Chandler, R.; Kendon, E.; Widmann, M.; Brienen, S.; Rust, H.; Sauter, T.; Themel, M.; et al. Precipitation downscaling under climate change: Recent developments to bridge the gap between dynamical models and the end user. *Rev. Geophys.* **2010**, *48*, RG3003. https://doi.org/10.1029/2009RG000314.
44. IPCC. *Climate Change 2021: The Physical Science Basis. Contribution of Working Group I to the Sixth Assessment Report of the Intergovernmental Panel on Climate Change*; Masson-Delmotte, V.P., Zhai, A., Pirani, S.L., Connors, C., Péan, S., Berger, N., Caud, Y., Chen, L., Goldfarb, M.I., Gomis, M., eds; Cambridge University Press: Cambridge, UK; New York, NY, USA, 2021, *in press*. https://doi.org/10.1017/9781009157896.
45. Lehner, F.; Deser, C.; Maher, N.; Marotzke, J.; Fischer, E.M.; Brunner, L.; Knutti, R.; Hawkins, E. Partitioning climate projection uncertainty with multiple large ensembles and CMIP5/6. *Earth Syst. Dynam.* **2020**, *11*, 491–508. https://doi.org/10.5194/esd-11-491-2020.
46. Camisay, M.F.; Rivera, J.A.; Matteo, L.; Morichetti, P.; Mackern, M.V.; Estimation of integrated water vapor from GNSS ground stations over Central-Western Argentina. Role in the development of regional precipitation events. *J. Atmosph. Sol. Terrest. Phys.* **2020**, *197*, 105143. https://doi.org/10.1016/j.jastp.2019.105143.
47. Garbarini, E.M.; González, M.H.; Rolla, A.L. The influence of Atlantic High on seasonal rainfall in Argentina. *Int. J. Climatol.* **2019**, *39*, 4688–4702. https://doi.org/10.1002/joc.6098.
48. Hurtado, S.I.; Agosta, E.A. El Niño Southern Oscillation-related precipitation anomaly variability over eastern subtropical South America: Atypical precipitation seasons. *Int. J. Climatol.* **2021**, *41*, 3793–3812. https://doi.org/10.1002/joc.6559.
49. Cabré, F.; Nuñez, M. Impacts of climate change on viticulture in Argentina. *Reg. Environ. Change* **2020**, *20*, 12. https://doi.org/10.1007/s10113-020-01607-8.